

Mixing Measures in Turbulent Channel Flow

Milind Singh

Department of Mechanical Engineering

McGill University, Montreal



December 2022

A thesis submitted to McGill University in partial fulfilment of the requirements
of the degree of Master of Engineering.

© Milind Singh, 2022

If we knew what it was that we were doing, it would not be called research, would it?

– Albert Einstein

Acknowledgements

First and foremost, I would like to thank Professor Laurent Mydlarski for being an outstanding supervisor and for giving me invaluable advice throughout the course of my research. He always found time in his busy schedule for meetings and answered all of my questions thoroughly. His generous help regarding all aspects of my project was crucial in improving the quality of my work. I have obtained a vast amount of knowledge from him in this field and I am extremely grateful for having been a part of his team. It would be an understatement to say that I could not have asked for a better supervisor for my work.

I would also like to extend my thanks to Dr. Emmanuel Germaine and Professor Luca Cortelezzi, who were always available to answer my questions and took time to offer insightful advice. Their assistance and willingness to make time for my questions was extremely appreciated for the duration of my research. The knowledge that I have gained from their insights is vast. I would also like to thank Sheldon Harrison for being a great friend, both on and off-campus, and for keeping me company throughout this degree.

I am grateful for my family, who constantly provided encouragement throughout my work. I am thankful for my parents' support and belief in me. My brother's support also provided me with motivation for the entire duration of my research. I would especially like to thank my grandfather, who inspired me to pursue the sciences. His support has been with me for as long as I can remember, and his words continue to inspire me in life.

Lastly, I would like to thank the National Sciences and Engineering Research Council of Canada (NSERC), Fonds de Recherche du Québec Nature et Technologies (FRQNT), and McGill University for funding this research through their scholarships over the course of my degree.

Contribution of Authors

All of the research presented in this thesis is my own work and I am a sole author of all of the chapters included in this thesis. I was provided guidance by Professor Mydlarski, Professor Luca Cortelezzi, and Dr. Emmanuel Germaine throughout the course of this research.

Abstract

Scalar mixing occurs within a wide variety of natural and engineering flows, the vast majority of which are turbulent. Predicting and controlling the scalar concentration(s) within these flows yields immediate benefits to numerous applications across many fields. To that extent, a better understanding of the effects of scalar-field initial conditions on the evolution(s) of the scalar concentration(s) is required to either promote or delay the rate at which the mixing occurs. Direct numerical simulations (DNSs) are employed herein to simulate the hydrodynamic and scalar fields as they resolve the full range of (length and time) scales in turbulent flows. A passive scalar, mixed by a fully developed turbulent channel flow, is considered. Mixing metrics (unmixedness and mix-norm) are used to quantify the mixing and observed differences in their evolution are explained by analyzing the different terms that comprise the scalar variance and scalar dissipation rate budgets. Temporal evolutions of the unmixedness and the mix-norm indicate that the fastest mixing occurs for the scalar-field initial condition in which the initial interface is aligned normal to the mean velocity vector (i.e., IC_x). It is also shown that the temporal evolution of the unmixedness is directly related to the scalar dissipation rate. For the IC_x initial condition, it is observed that higher production and destruction values of the scalar dissipation rate are a contributing factor to the rapid mixing. The strong advection and stretching of the interface by the mean flow in the IC_x case further leads to faster rates of scalar mixing. It is also observed that the anchoring of the interface(s) to the walls of the channel subjects them to enhanced turbulent activity, thus further promoting the rate at which mixing occurs. To promote mixing in a channel flow, it is recommended that scalar interfaces be aligned normal to the mean velocity vector.

Résumé

Le mélange de scalaires se produit dans une variété d'écoulements naturels et techniques, dont la grande majorité sont turbulents. La prédiction et le contrôle des concentrations scalaires au sein de ces flux offre des avantages immédiats à de nombreuses applications dans de nombreux domaines. Dans cette mesure, une meilleure compréhension des effets des conditions initiales du champ scalaire sur l'évolution des concentrations scalaires est nécessaire pour favoriser ou retarder la vitesse à laquelle le mélange se produit. Des simulations numériques directes (DNS) sont utilisées pour simuler les champs hydrodynamiques et scalaires puisqu'ils résolvent la gamme complète d'échelles (de longueur et de temps) des écoulements turbulents. Un scalaire passif, mélangé par un écoulement de canal turbulent pleinement développé, est étudié. Les métriques de mélange (*unmixedness* et *mix-norm*) sont utilisées pour quantifier le mélange. Les différences observées dans leurs évolutions sont expliquées en analysant les différents termes qui composent les budgets de variance du scalaire et de taux de dissipation scalaire. Les évolutions temporelles du *unmixedness* et du *mix-norm* indiquent que le mélange le plus rapide se produit pour la condition initiale de champ scalaire dans laquelle l'interface initiale est alignée perpendiculairement au vecteur de vitesse moyenne (IC_x). On montre que l'évolution temporelle du *unmixedness* est directement liée au taux de dissipation scalaire. Pour la condition initiale IC_x , on observe que des valeurs de production et de destruction plus élevées du taux de dissipation scalaire sont un facteur contribuant au mélange rapide. La forte advection et l'étirement de l'interface par le flux moyen dans le cas IC_x conduisent en outre à des taux plus rapides de mélange scalaire. On observe également que l'ancrage de la ou des interfaces aux parois du canal les soumet à une activité turbulente accrue, favorisant ainsi davantage la vitesse à laquelle se produit le mélange. Pour favoriser le mélange dans un écoulement de canal turbulent, il est recommandé que les interfaces scalaires soient alignées perpendiculairement au vecteur de vitesse moyenne.

Contents

1	INTRODUCTION	1
1.1	Background & Motivation	1
1.2	Objectives	4
1.3	Structure of the Thesis	5
2	THEORY & LITERATURE REVIEW	6
2.1	Basics of Turbulence	6
2.1.1	A Qualitative Description of Turbulence	6
2.1.2	A Statistical Description of Turbulence	8
2.2	Channel Flow	11
2.3	Advection & Diffusion of a Passive Scalar	14
2.4	Mixing Metrics	17
2.5	Literature Review	18
3	NUMERICAL METHODS	24
3.1	Direct Numerical Simulation of a Turbulent Channel Flow	25
3.1.1	Spatial Discretization of the Hydrodynamic Field	25
3.1.2	Temporal Discretization of the Hydrodynamic Field	29
3.2	Direct Numerical Simulation of Passive Scalar Transport	30
3.2.1	Spatial Discretization of the Scalar Transport Equation	31
3.2.2	Temporal Discretization of the Scalar Transport Equation	35
3.3	Boundary & Initial Conditions	37
3.4	Compute Canada Cluster	39
4	RESULTS	41
4.1	Averaging Schemes	41
4.2	Velocity Field	43

4.3	Scalar Field	44
4.3.1	Mixing Metrics	45
4.3.2	Scalar Variance Budget	50
4.3.3	Scalar Dissipation Rate Budget	52
4.4	Results Summary	58
5	CONCLUSION	59
5.1	Summary	59
5.2	Future Work	61
	REFERENCES	62

List of Figures

1	Schematic of a statistically one-dimensional channel.	11
2	Spatial discretization of the scalar transport equation.	32
3	Transport of the fluid volume, ΔV_p , over the time interval Δt	36
4	The three scalar-field initial conditions studied herein.	38
5	Mean streamwise component of the velocity field (a) and the root-mean-square (RMS) values of the three velocity field components (b) and comparisons with the work of Abe et al. (2001) and Germaine et al. (2014).	44
6	Concentration distributions generated at $\tau = 7$ by the action of the same turbulent channel flow on the three scalar-field initial conditions.	45
7	Time evolution of the unmixedness parameter (a) and the mix-norm (b) for the three scalar fields resulting from the three initial conditions.	46
8	Temporal evolution of the volume-averaged scalar dissipation rates for the scalar fields resulting from the three initial conditions.	48
9	Comparisons of the left hand side (LHS) and right hand side (RHS) of equation 17.	49
10	Temporal evolution of space- and time-averages of all 6 terms in the scalar variance budget.	51
11	Temporal evolution of the space- and time-averages of all 9 terms in the scalar dissipation rate budget in which statistical moments are assessed in planes parallel to the initial location of the interface in the initial condition.	53
12	Evolution in time of the time-averages of all 9 terms in the scalar dissipation rate budget in which statistical moments are assessed on the y - z plane at $x/L_x = 0.50$	54
13	Temporal evolution of the time-averages of all 9 terms in the scalar dissipation rate budget in which statistical moments are assessed on the x - z plane at $y/h = 1$	54
14	Temporal evolution of the time-averages of all 9 terms in the scalar dissipation rate budget in which statistical moments are assessed on the x - y plane at $z/L_z = 0.50$	54

- 15 Temporal evolution of the time-averages of all 9 terms in the scalar dissipation rate budget in which statistical moments are assessed on the mid-plane corresponding to the initial location of the interface in the initial condition. 56
- 16 Temporal evolution of the time-averages of all 9 terms in the scalar dissipation rate budget in which statistical moments are assessed in planes parallel to the initial location of the interface in the initial condition, but away from the mid-plane. . . . 57

List of Tables

- 1 Legend for the various terms in the budget of the scalar variance. 51
- 2 Legend for the various terms in the budget of the scalar dissipation rate. 55

1 INTRODUCTION

1.1 Background & Motivation

Scalar quantities (e.g., temperature, humidity, chemical species concentration) are mixed within a wide range of environmental and engineering flows (e.g., the atmosphere, which transports temperature and humidity; the oceanic mixed layer, in which temperature and salinity are mixed; chemical reactors; heat exchangers; combustion processes, etc.). Given that the vast majority of these flows are turbulent, an understanding of the turbulent scalar mixing process is required to predict (and, ultimately, control) these flows and the evolution of the concentration(s) of the scalar(s) therein.

The complex nature of the governing equations of fluid mechanics (i.e., non-linear partial differential equations with no known general solutions) makes the study of turbulent scalar mixing particularly difficult. Furthermore, the non-linear nature of the governing equations and their sensitivities to perturbations give rise to the chaotic and random behaviour observed in turbulent flows. Consequently, turbulent flows are difficult to predict, and thus statistical methods are used to quantify them and study their characteristics. As such, the study of any scalar quantity transported by a turbulent flow is also subject to the aforementioned features and thus requires a statistical approach.

Since the overwhelming majority of flows that are encountered in nature are inhomogeneous, the transport of a scalar quantity in such a flow is of particular interest due to its ubiquitous nature. The work presented herein focuses on the mixing of a passive scalar in a turbulent channel flow (the simplest realization of an inhomogeneous flow) by means of direct numerical simulations (DNSs), where the term “passive” denotes that the scalar does not influence the dynamics of the fluid flow, allowing for independent treatment of the hydrodynamic field and the scalar fields that it mixes. Such an assumption is reasonable and valid in many physical flows (e.g., situations where temperature fluctuations are sufficiently small) and will be used for the DNSs conducted in this work.

One of the most significant advantages of DNS is that it allows for the resolution of all scales of the flow without relying on the use of any turbulence models, as is the case for other computational methods such as Reynolds-Averaged Navier-Stokes (RANS) approaches or Large Eddy Simulation (LES). As such, both the turbulent velocity and scalar fields studied in this work are computed using the DNS approach. The turbulent velocity field is calculated using a spectral method, while the scalar field is calculated using a flux integral method.

The scalar mixing process to be studied herein requires a simulation of the transport of the scalar quantity by the bulk motion of the fluid (i.e., advection) and its transport by molecular processes (i.e., molecular diffusion). It is the latter that is ultimately responsible for destroying (i.e., dissipating) any turbulent scalar fluctuations and thus gradually removing any differences in scalar concentrations. Due to its presence in any turbulent flow mixing scalars, the scalar dissipation is of particular interest in better understanding the processes by which the mixing occurs. As it stands, the physical mechanisms behind the dissipation process remain unclear and require further study.

Evolution of the scalar variance and its destruction by the scalar dissipation rate can be better understood by examining the physical processes that govern their production, transport, and destruction. These processes are described by the scalar variance and scalar dissipation rate evolution equations (i.e., “budgets”). The biggest challenge in analyzing these equations, however, stems from the fact that several of the terms in both of the evolution equations require simultaneous measurements of the velocity and scalar fields. This challenge is addressed through the use of DNSs in the present work, which resolve the velocity and scalar fields at identical spatial and temporal coordinates. By overcoming the hurdles of analyzing the scalar variance and scalar dissipation rate budgets, one can gain additional insight into the processes that dominate the evolution of the scalar variance and the scalar dissipation rate, and thus better understand the mixing process as a whole.

While the scalar dissipation rate is one of the most important metrics commonly used to describe the mixing in turbulent flows, there does not exist a universally accepted metric that is used

to quantify the scalar mixing process. Through necessity, however, different mixing metrics have been proposed over the years to describe different phenomena. These include the “stirring” and “mixing” processes which are distinctly different and require different approaches in describing them. Stirring is a mechanical action that creates filaments of scalar concentration, whereas mixing is a diffusion driven process which smooths out the differences in scalar concentrations amongst these filaments (Thiffeault, 2012). Since stirring is an action that does not alter the scalar variance, but rather redistributes it within the flow at various scales, it requires a metric capable of factoring in the length scales of the mixing process. Mixing, however, can be described using a measurement of the scalar variance.

Combined with the scalar dissipation rate, the use of different mixing metrics can offer insight into the evolution of a system from an unmixed state to a mixed one, and the physical processes that partake in the mixing. The path that a system takes in approaching the mixed state can vary based on a number of factors. One of these factors is the starting state of the system (i.e., the initial condition), which can determine the rate at which mixing occurs (Gubanov and Cortelezzi, 2009). Consequently, a better understanding of how to orient and/or construct the initial scalar field to achieve the desired rate of mixing can be advantageous in many fields. Immediate applications may include processes where the rapid mixing of scalars yields numerous benefits, such as the mixing of fuel and air in combustion engines, the mixing of heat in heat exchangers, or the mixing of various chemical reactants and/or products in chemical reactors.

Therefore, to further our understanding of turbulent scalar mixing, it is beneficial to address the fact that the effects of scalar-field initial conditions on the mixing process are not yet fully understood. The focus of this thesis is to examine the evolutions of various scalar-field initial conditions as they are mixed by identical hydrodynamic fields. Effects of the initial conditions on the mixing process will be quantified using different mixing metrics, the scalar dissipation rate, and the budget equations which govern the evolutions of the scalar variance and the scalar dissipation rate.

1.2 Objectives

As previously discussed, the present work aims to better understand the mechanisms that underlie the scalar mixing process in a turbulent channel flow. The complexity of the task at hand requires this analysis to be conducted using various mixing metrics and scalar “budgets.” Relationships between these metrics and the physical processes will provide insight into the different mixing behaviours resulting from the different initial conditions. The major objectives for this work are specified as follows:

1. Perform DNSs for three initial scalar-field geometries subjected to the action of identical fully-developed, high-aspect-ratio, turbulent channel flows.
2. Analyze the evolutions of the scalar dissipation rates for the different scalar-field initial conditions as functions of time.
3. Quantify the mixing and stirring efficiencies using the unmixedness parameter (Danckwerts, 1952; Dimotakis and Miller, 1990) and the mix-norm (Mathew et al., 2005), and study their evolutions for different scalar-field initial conditions.
4. Calculate and analyze the various terms in the scalar variance and scalar dissipation rate budgets to better understand the physical processes and mechanisms that underlie the scalar mixing process.
5. Attribute the differences in the evolutions of the scalar dissipation rates and mixing metrics to the physical mechanisms examined in the scalar budget equations.
6. Draw conclusions regarding the mixing process of a passive scalar in a turbulent channel flow and its dependence on initial conditions.

The methodology for completing the aforementioned objectives is discussed in-depth in the work presented herein. To this end, the following subsection will provide the reader with an overview of the structure of this thesis.

1.3 Structure of the Thesis

Theory pertaining to the description of turbulence is first presented in chapter 2, to familiarize the reader with the concepts and underlying theories of turbulence. Both qualitative and statistical overviews of turbulence are provided in section 2.1. Further background specific to turbulent channel flow is provided in section 2.2, followed by a discussion of the advection and diffusion of a scalar quantity in section 2.3. A discussion of the mixing metrics that will be used in this work to quantify the molecular mixing and stirring is given in section 2.4. Lastly, in section 2.5, the literature pertaining to the effect of scalar field initial conditions is reviewed.

An overview of the numerical methodology is provided in chapter 3. Section 3.1 describes the code used to conduct the DNS for the hydrodynamic (velocity) field, and provides the reader with a description of the spectral method used for this DNS. Simulation of the advection and diffusion of a passive scalar by the previously computed velocity field is discussed in section 3.2. Details are provided for the flux-integral method which is used to solve the advection-diffusion equation in three-dimensions. The boundary and initial conditions for the simulations are discussed in section 3.3. The Compute Canada cluster that was used to conduct the simulations is detailed in section 3.4.

The results are presented in chapter 4. A thorough discussion of the averaging schemes used is first discussed in section 4.1 to provide the reader with a better understanding of the results. Results for the hydrodynamic field are validated in section 4.2. Evolutions of the mixing metrics and scalar dissipation rates, as well as all terms in the scalar variance and scalar dissipation rate budgets, are analyzed for the three different scalar-field initial conditions in section 4.3. A summary of the results is presented in section 4.4.

A final chapter is presented with concluding remarks and discussion of future work to be conducted to further expand upon the work presented herein in sections 5.1 and 5.2, respectively.

2 THEORY & LITERATURE REVIEW

The ubiquitous nature of turbulence makes its study particularly beneficial, as its applications are profound. The following sections serve to provide the reader with background theory pertaining to turbulence and the mixing of passive scalars therein.

2.1 Basics of Turbulence

2.1.1 A Qualitative Description of Turbulence

Laminar flows, which are characterized by high viscosities, low velocities, and/or small dimensions, are infrequently observed in natural and engineering applications. A practical way to describe turbulence is by differentiating it from laminar flow and by discussing some of its qualitative characteristics (Tennekes and Lumley, 1972):

- Irregularity - first and foremost, the obvious distinction between laminar and turbulent flows arises from the chaotic and random fluctuations of fluid properties of the latter, making it very difficult to predict.
- Vorticity - the rotational nature of turbulent flows produces high levels of vorticity fluctuations. The existence of these fluctuations in three dimensions makes them subject to the phenomenon of vortex stretching.
- Dissipation - a continuous supply of energy is required to offset the kinetic energy losses that ensue as a result of deformation work performed by the viscous shear stresses in turbulent flows. A rapid decay of kinetic energy associated with the turbulent velocity fluctuations will be observed if the energy supply is disrupted.
- Diffusivity - the rapid mixing and increased rates of mass, momentum, and energy transfer are of particular importance in turbulent flows. The diffusive nature of turbulence has significant consequences, such as increased heat transfer rates in heat exchangers, or the ability to delay separation of turbulent boundary layers through the mixing of momentum.
- Turbulent flows are flows - it should be noted that turbulence is a feature that stems from the

fluid flow, rather than being a property of the fluid itself. As such, each turbulent flow will exhibit characteristics that are dependent upon the initial and boundary conditions imposed on the flow. Since the equations of motion (to be discussed shortly) are non-linear partial differential equations and do not have known general solutions, the study of turbulence is enhanced by focusing on certain groups and classes of turbulent flows.

The characteristics discussed above are reflective of some of the commonly observed qualities of turbulence. Another crucial aspect of turbulent flows is the notion of an **energy cascade** that is responsible for distributing turbulent kinetic energy amongst the various scales of the flow. Discussion of the aforementioned scales of turbulence is best presented when the topic of the energy cascade is coupled with the Kolmogorov hypotheses (to be discussed shortly).

In describing the energy cascade, the first observation to be made is that turbulent flows contain eddies of various sizes. Although an eddy has no exact, universal definition, it can be regarded as a localized and coherent structure exhibiting a rotational turbulent motion. At large scales, these eddies are of sizes and scales comparable to those of the geometry of the flow, and the effects of viscosity at these large scales can generally be neglected. Due to instabilities, however, these large eddies break down into eddies of smaller sizes, which further break up into eddies of smaller sizes still. In this manner, energy is transferred continuously from large to small scales through eddies of decreasing sizes. This trend continues until the smallest (Kolmogorov) scales of the flow are reached, at which the kinetic energy is dissipated by the actions of the molecular viscosity. The smallest scales of the flow, as well as their spatial/temporal dependence, are addressed by Kolmogorov theory, which consists of one postulate and two hypotheses (Kolmogorov, 1941).

The first component of this theory, referred to as the postulate of local isotropy, states that the geometric information of large-scale eddies is lost as energy is transferred down the cascade. As a consequence, Kolmogorov suggested that the smallest scales are locally isotropic and are statistically universal for all turbulent flows at high Reynolds numbers. Kolmogorov's first hypothesis, states that for sufficiently high Reynolds numbers, scales sufficiently smaller than the largest scales

of the flow are dependent entirely upon the rate of dissipation of turbulent kinetic energy and the kinematic viscosity of the fluid. His second hypothesis, states that for eddies of sizes in between the largest and smallest of the flow, the motions are functions of only the dissipation rate, and the effects of viscosity are negligible.

2.1.2 A Statistical Description of Turbulence

There are two equations in fluid mechanics which govern the velocity (hydrodynamic) field. The first governing equation that pertains to the hydrodynamic field is a statement of conservation of mass, and is commonly referred to as the continuity equation. Assuming constant properties, it is written as a non-divergence statement:

$$\frac{\partial \tilde{u}_i}{\partial x_i} = 0, \quad (1)$$

where \tilde{u}_i is the instantaneous velocity. The second (set of) governing equations are the Navier-Stokes equations. These are derived from Newton's Second Law, and are commonly written in the form (also assuming constant properties):

$$\frac{\partial \tilde{u}_i}{\partial t} + \tilde{u}_j \frac{\partial \tilde{u}_i}{\partial x_j} = -\frac{1}{\rho} \frac{\partial \tilde{p}}{\partial x_i} + g_i + \nu \frac{\partial^2 \tilde{u}_i}{\partial x_j \partial x_j}, \quad (2)$$

where ρ is the fluid density, \tilde{p} is the instantaneous pressure, and g_i are external body forces. The Navier-Stokes equations are a statement of conservation of momentum, and express the notion that the rate of change of the velocity of a fluid particle is equal to the sum of the pressure forces acting in the respective direction, any external forces (e.g., gravity), and the dissipative viscous forces acting on the fluid. Since equations 1 and 2 govern the motion of a fluid in a given (constant-property) flow, their solutions are of critical importance in understanding and predicting turbulent flows. The most significant challenge posed in the study of turbulence stems from the fact that equation 2 has no known general solutions in three dimensions at high Reynolds numbers. Therefore, numerical solutions of equations 1 and 2 via direct numerical simulation (DNS) will be used in this work.

Although the governing equations of fluid mechanics (and thus of turbulence) are determin-

istic, turbulence is most frequently studied as a stochastic process, because the sensitivities of the governing equations to perturbations in the initial conditions can result in a different realization of the flow with even the smallest of differences in the starting conditions. As such, turbulent variables are treated as random variables and a statistical approach is utilized in performing meaningful analyses that can be extended to similar flows.

The primary variable to consider in the study of turbulent flows is the fluid's velocity. Treatment of the velocity as a random variable is initiated by the application of the so-called Reynolds decomposition, such that the instantaneous velocity (\tilde{u}_i) is decomposed into a mean component (U_i) and a turbulent fluctuation about this mean (u_i), in the following manner:

$$\tilde{u}_i \equiv U_i + u_i.$$

This deconstruction of the instantaneous velocity is useful, as it allows for the discussion of the mean velocity, as well as the turbulent fluctuations, which are integral to our study of turbulent flows and the mixing therein. The mean velocity of the flow can be used to define a (bulk) **Reynolds number**, which is the primary dimensionless number that is used throughout fluid mechanics, and is given as:

$$Re = \frac{UL}{\nu},$$

where L is a characteristic length of the flow, and ν is the kinematic viscosity of the fluid. The Reynolds number describes the ratio of inertial forces to the viscous forces of a flow, and higher values of this ratio are associated with turbulent flows. It can then be inferred that turbulent flows are dominated by inertial forces, which leads to instabilities.

Instabilities, such as the aforementioned eddies, are responsible for transferring the turbulent kinetic energy (TKE) amongst the various scales of the flow. The TKE, defined as $\frac{1}{2}\langle u_i u_i \rangle$, is produced at the largest (integral) scales and is transferred down to the smallest (Kolmogorov) scales, where it is dissipated by viscous forces. The production, transport, and destruction of the TKE is governed by the TKE evolution equation (i.e., TKE budget), and is written in the form:

$$\begin{aligned}
\underbrace{\frac{\partial}{\partial t} \langle \frac{1}{2} u_i u_i \rangle}_{(i)} + \underbrace{U_j \frac{\partial}{\partial x_j} \langle \frac{1}{2} u_i u_i \rangle}_{(ii)} = & - \underbrace{\frac{\partial}{\partial x_j} \langle \frac{1}{\rho} u_j p \rangle}_{(iii)} - \underbrace{\frac{\partial}{\partial x_j} \langle u_i u_i u_j \rangle}_{(iv)} + \underbrace{2\nu \frac{\partial}{\partial x_j} \langle u_i s_{ij} \rangle}_{(v)} \\
& - \underbrace{S_{ij} \langle u_i u_j \rangle}_{(vi)} - \underbrace{2\nu \langle s_{ij} s_{ij} \rangle}_{(vii)},
\end{aligned} \tag{3}$$

where angular brackets ($\langle \cdot \rangle$) denote averaging and S_{ij} is the mean rate of strain, defined as:

$$S_{ij} = \frac{1}{2} \left(\frac{\partial U_i}{\partial x_j} + \frac{\partial U_j}{\partial x_i} \right),$$

and s_{ij} is the fluctuating rate of strain, defined as:

$$s_{ij} = \frac{1}{2} \left(\frac{\partial u_i}{\partial x_j} + \frac{\partial u_j}{\partial x_i} \right).$$

The (averaged) TKE budget (i.e., equation 3) states that the time-rate of change of TKE (i) and the advection of TKE by the mean flow (ii) is governed by the transport of TKE by the pressure gradient (iii), transport by turbulent velocity fluctuations (iv), transport by viscous stresses (v), as well as the production of TKE (vi), and the dissipation (destruction) of TKE (vii) (Tennekes and Lumley, 1972). The final term (vii) in equation 3 is called the **dissipation rate** of TKE, and is denoted by $\langle \varepsilon \rangle \equiv 2\nu \langle s_{ij} s_{ij} \rangle$.

The dissipation rate of TKE, $\langle \varepsilon \rangle$, describes the rate at which turbulent kinetic energy is converted into internal energy by viscous effects. The conversion of TKE to internal energy occurs at the smallest (Kolmogorov) scales, where the effects of viscosity are most dominant. Naturally, the kinetic energy dissipation rate is then used to quantify the Kolmogorov scales, which are defined as:

$$\eta \equiv (\nu^3 / \varepsilon)^{1/4},$$

$$u_\eta \equiv (\varepsilon \nu)^{1/4}, \text{ and}$$

$$\tau_\eta \equiv (\nu/\varepsilon)^{1/2}.$$

These values describe the length, velocity, and time scales, respectively, of the smallest eddies in the flow. It should be noted that the local Reynolds number associated with these scales is unity, given that:

$$Re = \frac{u_\eta \eta}{\nu} = 1.$$

Thus, at these smallest scales, viscous effects become significant and are responsible for dissipating the kinetic energy.

2.2 Channel Flow

Most flows that are encountered in natural and engineering applications are inhomogeneous, and the focus of the research in this thesis is thus on the mixing of a scalar in such a flow. Channel flow is a type of wall-bounded flow and is the simplest realization of an inhomogeneous flow. Specifically, the work herein considers the scalar mixing within a fully-developed, statistically one-dimensional, turbulent channel flow.

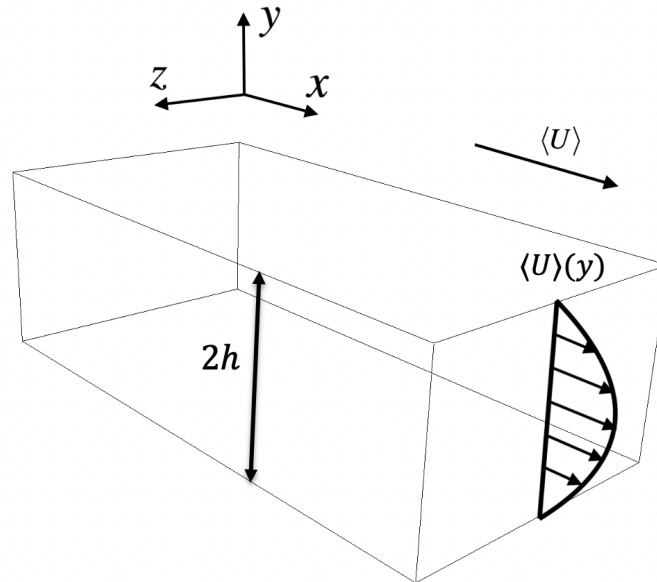


Figure 1: Schematic of a statistically one-dimensional channel.

The components of the instantaneous velocity defined in the x , y , and z directions are \tilde{u} , \tilde{v} ,

and \tilde{w} , respectively. As depicted in figure 1, the mean flow occurs in the streamwise (x) direction, and is bounded by two walls separated by a distance $2h$ normal to the wall-normal (y) direction. The extent of the channel in the streamwise (x) and spanwise (z) directions is large compared to that of the wall-normal direction and thus the flow is (statistically) one-dimensional. Since the flow is also statistically steady, the mean velocity is only a function of the wall-normal direction (i.e., $\langle U \rangle = \langle U \rangle(y)$ only).

For channel flow, the Reynolds number is defined using the mean streamwise velocity measured at the channel half-height, h , such that:

$$Re_{D_h} = \frac{UD_h}{\nu},$$

where D_h is the hydraulic diameter defined as 4 times the ratio of the cross-sectional channel area to the wetted perimeter, so that $D_h = 4A_{c.s.}/P_w = 4h$. For $Re \gtrsim 2300$, the flow is fully turbulent (Pope, 2000).

The shear stress that is exerted by the fluid on the walls is an important parameter in such a wall-bounded flow and is given by:

$$\tau_w \equiv \rho\nu \left(\frac{d\langle U \rangle}{dy} \Big|_{y=0} \right).$$

The shear stress at the wall is entirely a result of viscous contribution given the no-slip and no-penetration boundary conditions. Near the wall, the fluid viscosity, ν , and the wall shear-stress, τ_w , are prominent quantities (Gubian et al., 2019). As a result, these variables are used to formulate important viscous scales that are frequently used in the study of channel flow.

The first of these viscous scales is the velocity scale in the near-wall region, called the **friction velocity**, which is expressed as:

$$u_\tau \equiv \sqrt{\frac{\tau_w}{\rho}} = \sqrt{\nu \frac{d\langle U \rangle}{dy} \Big|_{y=0}},$$

and the second viscous scale is the **viscous lengthscale**, defined as:

$$\delta_\nu \equiv \frac{\nu}{u_\tau}.$$

Using either the friction velocity or the viscous lengthscale, we can define a **friction based Reynolds number**, commonly used to quantify the level of turbulence in channel flows, as:

$$Re_\tau \equiv \frac{h}{\delta_\nu} = \frac{u_\tau h}{\nu}.$$

Additionally, the distance from the wall can be measured in terms of **viscous lengths**, or wall units, defined using either the friction velocity or viscous lengthscale:

$$y^+ \equiv \frac{y}{\delta_\nu} = \frac{u_\tau y}{\nu},$$

where the superscript “+” denotes normalization by viscous scales.

The use of friction-based scales also allows for the formulation of a *law of the wall*, which describes the shape of the velocity profile at varying distances from the wall. To better understand this concept, we first introduce a non-dimensional velocity:

$$U^+ = \frac{U}{u_\tau},$$

which depends on the wall-normal distance (y^+). Dominance of viscous effects in the near-wall ($y^+ < 5$) region yields a layer termed the **viscous sublayer**, where the velocity profile is a linear function of the wall-normal distance:

$$U^+ = y^+.$$

With increasing distance from the wall, turbulence begins to dominate over viscous effects. This region is termed the **log-law region** ($y^+ > 30, y/h < 0.3$), over which the velocity profile is a

logarithmic function of the viscous length:

$$U^+ = \frac{1}{\kappa} \ln y^+ + B,$$

where $\kappa = 0.41$ is the von-Kármán constant, and $B = 5.2$ is a constant. The region in between the viscous sublayer and the log-law region is called the **buffer layer** ($5 < y^+ < 30$), and represents a transition from the viscosity-dominated region to the turbulence-dominated region of the channel. The region represented by $y^+ > 50$ is termed the **outer layer**, and is the region where the direct effects of viscosity on the mean velocity profile are negligible (Pope, 2000). In the central part of the channel ($0.3 \leq y/h \leq 1.0$), there are deviations in the mean velocity profile from the log-law due to the velocity defect law. The velocity defect (F_D) is the difference between the mean velocity, U , and the centerline velocity, U_c . The velocity defect law states that the velocity defect normalized by the friction velocity is a function of y/h only, such that:

$$F_D \left(\frac{y}{h} \right) = \frac{U_c - U}{u_\tau}.$$

Unlike the log-law function, however, F_D does not have a universal form and is different for different flows.

2.3 Advection & Diffusion of a Passive Scalar

The mixing of scalars in turbulence is governed by the advection-diffusion equation, commonly written (assuming constant properties) in the form:

$$\frac{\partial \tilde{\theta}}{\partial t} + \tilde{u}_j \frac{\partial \tilde{\theta}}{\partial x_j} = \alpha \frac{\partial^2 \tilde{\theta}}{\partial x_j \partial x_j}, \quad (4)$$

where $\tilde{\theta}$ is the instantaneous value of the scalar quantity, and α is the molecular diffusivity of the scalar. The advection-diffusion equation (also called the scalar transport equation) states that the sum of the time rate of change of the scalar and its advection by the flow is equal to the molecular

diffusion of the scalar quantity. Similar to the Navier-Stokes equations, the advection-diffusion equation has no known general solution in the context of turbulent velocity fields.

Similar to the Reynolds decomposition that was performed on the instantaneous velocity in section 2.1.2, the instantaneous value for the scalar ($\tilde{\theta}$) can be decomposed into a mean component (Θ) and a turbulent fluctuation about this mean (θ), such that:

$$\tilde{\theta} \equiv \Theta + \theta.$$

Upon substituting this decomposition into the advection-diffusion equation, one can derive the evolution equation (i.e., budget) for the **scalar variance**, $\langle \theta^2 \rangle$, which describes the contributions of various physical mechanisms to the evolution of the scalar variance and is the scalar analog of the TKE budget:

$$\underbrace{\frac{\partial}{\partial t} \langle \frac{1}{2} \theta^2 \rangle}_{(i)} + \underbrace{U_j \frac{\partial}{\partial x_j} \langle \frac{1}{2} \theta^2 \rangle}_{(ii)} = - \underbrace{\frac{\partial}{\partial x_j} \langle \frac{1}{2} u_j \theta^2 \rangle}_{(iii)} + \underbrace{\alpha \frac{\partial^2}{\partial x_j^2} \langle \frac{1}{2} \theta^2 \rangle}_{(iv)} - \underbrace{\langle u_j \theta \rangle \frac{\partial \Theta}{\partial x_j}}_{(v)} - \underbrace{\alpha \langle \frac{\partial \theta}{\partial x_j} \frac{\partial \theta}{\partial x_j} \rangle}_{(vi)}. \quad (5)$$

The scalar variance is a particularly useful quantity in that it quantifies the (square of the) average magnitude of turbulent scalar fluctuations in the flow. Equation 5 expresses that the time rate of change (i) and the advection of the scalar variance by the mean flow (ii) are balanced by its turbulent and molecular transport ($iii + iv$), production (v), and destruction (i.e., dissipation) (vi).

The last term in equation 5 is called the **scalar dissipation rate**, $\langle \varepsilon_\theta \rangle \equiv \alpha \langle \frac{\partial \theta}{\partial x_j} \frac{\partial \theta}{\partial x_j} \rangle$, and describes the rate at which the scalar variance is destroyed. Furthermore, this is the most important term in all of scalar turbulence, as it is the only term that appears in all turbulent flows in which scalars are mixed. These qualities of $\langle \varepsilon_\theta \rangle$ make it very relevant in the work presented herein regarding the mixing of a passive scalar. Further insight into the evolution of $\langle \varepsilon_\theta \rangle$ can be gained

by deriving the budget for the scalar dissipation rate from the advection-diffusion equation:

$$\begin{aligned}
\underbrace{\frac{\partial \langle \varepsilon_\theta \rangle}{\partial t}}_{(i)} + \underbrace{U_j \frac{\partial \langle \varepsilon_\theta \rangle}{\partial x_j}}_{(ii)} = & -2\alpha \underbrace{\frac{\partial U_j}{\partial x_i} \langle \frac{\partial \theta}{\partial x_i} \frac{\partial \theta}{\partial x_j} \rangle}_{(iii)} - 2\alpha \underbrace{\frac{\partial \Theta}{\partial x_j} \langle \frac{\partial u_j}{\partial x_i} \frac{\partial \theta}{\partial x_i} \rangle}_{(iv)} - 2\alpha \underbrace{\langle u_j \frac{\partial \theta}{\partial x_i} \rangle \frac{\partial^2 \Theta}{\partial x_i \partial x_j}}_{(v)} \\
& - 2\alpha \underbrace{\langle \frac{\partial u_j}{\partial x_i} \frac{\partial \theta}{\partial x_i} \frac{\partial \theta}{\partial x_j} \rangle}_{(vi)} + \alpha \underbrace{\frac{\partial^2 \langle \varepsilon_\theta \rangle}{\partial x_j^2}}_{(vii)} - \underbrace{\frac{\partial}{\partial x_j} \langle u_j \varepsilon_\theta \rangle}_{(viii)} - 2\alpha^2 \underbrace{\langle \frac{\partial^2 \theta}{\partial x_i \partial x_j} \frac{\partial^2 \theta}{\partial x_i \partial x_j} \rangle}_{(ix)}. \tag{6}
\end{aligned}$$

Equation 6 states that the time rate of change (i) and advection of $\langle \varepsilon_\theta \rangle$ by the mean flow (ii) are governed by the production of $\langle \varepsilon_\theta \rangle$ due to mean velocity gradients (iii), production due to mean scalar gradients (iv), mixed production (v), production due to turbulent vortex stretching (vi), as well as the molecular and turbulent transport of $\langle \varepsilon_\theta \rangle$ (vii + viii), and the dissipation (destruction) of $\langle \varepsilon_\theta \rangle$ (ix).

Analysis of the individual terms in equations 5 and 6 will provide insight into the various physical phenomena that govern the evolutions of the scalar variance and the scalar dissipation rate, and consequently that of the turbulent scalar mixing process. Lastly, it is beneficial to familiarize the reader with the smallest scalar length scale that exists in a flow. This scalar scale (η_θ) is related to the smallest hydrodynamic scale (η) by the **Prandtl number**, which measures the ratio of kinematic viscosity to the scalar's molecular diffusivity:

$$Pr = \frac{\nu}{\alpha}.$$

For the fluid and scalar considered herein (i.e., air and temperature, respectively), this value is $Pr = 0.7$, and the relationship between the smallest hydrodynamic scale (η) and the smallest scalar scale (η_θ) is expressed as:

$$\eta_\theta = \frac{\eta}{Pr^{3/4}}.$$

Since $Pr < 1$, $\eta_\theta > \eta$. Moreover, the smallest scalar scale (η_θ) in this case is called the **Corrsin scale** (Corrsin, 1951) and is the same order of magnitude as the Kolmogorov scale (η) given that the Prandtl number in air is close to unity.

It should be noted that the scalar considered in the work herein is a passive scalar, where the term “passive” denotes that the scalar does not influence the dynamics of the fluid flow. It is valid to consider temperature as a passive scalar if the ratio of the buoyant production to the dissipation rate of the TKE is small (i.e., if $\frac{g}{\Theta} \langle w\theta \rangle$ is small) (Tennekes and Lumley, 1972).

2.4 Mixing Metrics

Mixing metrics are often used to quantify the scalar mixing process. While there exists no universally accepted metric, two different measures are employed herein that have been previously used to study the mixing process. The use of such measures quantifies the state of the scalar field’s distribution at any instance in time with respect to some reference state (i.e., the uniformly mixed state in which the scalar variance is zero).

The first mixing metric to be considered is the **unmixedness** (Danckwerts, 1952; Dimotakis and Miller, 1990), which is defined in terms of the scalar variance and the mean scalar concentration, such that:

$$\Xi \equiv \frac{\langle \theta^2 \rangle}{\Theta(1 - \Theta)}; \quad 0 \leq \Xi \leq 1, \quad (7)$$

where θ has been normalized to be bounded between 0 and 1. The unmixedness is a non-dimensional measure of molecular mixing (primarily a small-scale process) and describes the relative magnitude of the scalar variance with respect to the mean scalar concentration. The maximum value for Ξ (i.e., $\Xi = 1$) represents a state of maximum separation of the scalar variance from the mean scalar concentration, whereas its minimum value (i.e., $\Xi = 0$) represents a state in which the scalar variance is non-existent (i.e., the scalar has been completely mixed). Although the unmixedness is a good measure of the molecular mixing in the flow, its drawback is that it contains no information regarding the scales at which the mixing process occurs.

This issue is addressed by the second mixing metric used herein, entitled the **mix-norm**

(Mathew et al., 2005):

$$\mu_\theta = \left[\sum_{\mathbf{k} \in \mathbb{Z}^3} \frac{1}{\sqrt{1 + 4\pi^2 \|\mathbf{k}^2\|}} |\hat{\Theta}_{\mathbf{k}}(t)|^2 \right]^{1/2}; \mu_\theta \geq 0, \quad (8)$$

where \mathbf{k} is the wavenumber and $\hat{\Theta}_{\mathbf{k}}$ are the spectral coefficients of the scalar fluctuations. Unlike the unmixedness, the mix-norm (μ_θ) is a multi-scale measure and accounts for the scales at which the scalar fluctuations are distributed. The denominator in equation 8 acts as a weighting function, such that for scalar fluctuations distributed at large scales (i.e., small \mathbf{k}), the denominator is small and thus μ_θ is large, while for distributions of the scalar fluctuations at smaller scales (i.e., large \mathbf{k}), the denominator is large and thus μ_θ is small. As a consequence of this multi-scale measure, μ_θ is able to account for mixing at all scales of the flow.

Note that the two aforementioned metrics are very different: the unmixedness, Ξ , quantifies molecular mixing (primarily a small-scale process) only, whereas the mix-norm, μ_θ , quantifies mixing by accounting for both stirring (generally a large-scale process) and molecular mixing. These differences have an impact on the results. For example, consider the idealized case of mixing in two dimensions of two hypothetical fluids (one white and one black, and both having molecular diffusivities equal to zero). Let one then assume that the fluid could be mixed in such a way that the end result would be a configuration similar to a chessboard, with white and black squares at the smallest scales. In this case, the unmixedness would be maximum and equal to one (because there is no molecular mixing) whereas the mix-norm will be minimum, because the stirring is complete.

2.5 Literature Review

Scalar mixing has been a topic of extensive research over the years due to its prominence in natural and engineering applications alike. One of the earliest noteworthy contributions to the study of turbulence comes from Richardson (1922), who first proposed the notion of a turbulent energy cascade and suggested that turbulent flows are comprised of eddies of various sizes. Eddies that exist at the largest scales of the flow break up into eddies of smaller sizes due to instabilities, which

break up into eddies of smaller sizes still. This process continues until the smallest scales of the flow are reached, where the kinetic energy of the eddies is dissipated via viscous effects.

Since the largest scales of the flow are dependent upon the geometry of the flow, there does not exist a theory that universally describes these large scales. Kolmogorov (1941) argued, however, that information regarding the large scales is lost as eddies break up and travel down the energy cascade. Thus, he suggested that, at sufficiently high Reynolds numbers, the small scales for all turbulent flows are statistically isotropic, homogeneous, and universal. The work of Kolmogorov was highly influential in the study of turbulence and inspired many new theories in the field.

As a natural extension of Kolmogorov's work, it was proposed that the advection of a scalar field by a turbulent flow would also exhibit similar universal characteristics at small scales (Obukhov, 1949; Corrsin, 1951; Batchelor, 1959; Monin and Yaglom, 1971). The Kolmogorov-Obukhov-Corrsin (KOC) theory (Kolmogorov, 1941; Obukhov, 1949; Corrsin, 1951) is the most prevalent theory related to turbulent scalar mixing, and predicts that the smallest scales of the scalar field should be statistically isotropic and independent of the largest scales of the the scalar field.

The work of Sreenivasan (1991) examined the degree to which the expected local isotropy and universality applied to scalar fields. In his findings, he stated that the asymptotic state of the scalar field was reached very slowly in shear flows as the Reynolds number increased, and that diffusive effects were relevant in the inertial subrange, even at large Reynolds numbers. Although Sreenivasan reported that local isotropy (for scalars) was not naturally present in shear flows, he did not entirely dismiss the possibility of local isotropy being attained at extremely large Reynolds numbers. He did state, however, that such large Reynolds numbers would be rare in terms of flows observed on Earth, whether they be natural or man-made.

Direct numerical simulation (DNS) of passive scalar mixing by a velocity field in the presence of an imposed mean gradient was conducted by Pumir (1994). By studying the skewness of the probability density functions (PDFs) of the scalar gradient, he revealed the presence of strong anisotropy. Furthermore, he observed sharp maxima of the scalar gradient, suggesting strong mix-

ing in large regions, and occurrences of small regions with strong scalar gradients. Although these results further supported arguments of anisotropic small-scales, they did not address the question of local isotropy of scalar fields when approaching infinite Reynolds numbers.

The notion of local scalar isotropy in the limit of infinite Reynolds numbers was challenged by Warhaft (2000). Through the use of third-moment statistics (skewness), he showed that there was an absence of isotropy at both the inertial and dissipation ranges in the scalar field and demonstrated the presence of strong intermittency in the inertial subrange in the scalar field. Findings from his work suggested that the large-scale properties of the scalar field were directly reflected onto its small-scales.

It is already well known that the chaotic action of turbulence is critical to mixing, and that faster mixing is achieved by a flow undergoing transition to, or halting in, a turbulent regime (Dimotakis, 2000). It has also been demonstrated in free shear flows that the initial conditions of a scalar field have a notable impact on its evolution (Beaulac and Mydlarski, 2004a; Lepore and Mydlarski, 2009). Given the above context relating to scalar mixing in turbulent flows, the specific motivation for the present work stems from the observations of Gubanov and Cortelezzi (2009) and Germaine et al. (2018), who noted that scalar fields, including the scalar dissipation rate, were strongly affected by the initial conditions of the scalar field, even when these scalar-field initial conditions were mixed by identical hydrodynamic fields. It is therefore of interest to study and investigate the nature of the physical processes that lead to such different evolutions of the scalar field.

Gubanov and Cortelezzi (2009) addressed the problem of designing a mixing device capable of maintaining a uniform mixing quality for different scalar-field initial conditions in laminar flow. In their work, they considered a two-dimensional sine flow, in which they promoted mixing by generating an optimized stirring protocol via the short time horizon procedure. To quantify the measure of mixing efficiency, the authors used the mix-norm (Mathew et al., 2005) as their mixing metric. Results from their study indicated that for short switching times, the optimized mixing

protocols were insensitive to the initial geometries of the scalar field, whereas for larger switching times, the optimized mixing protocols were more sensitive to the initial geometries when compared to benchmark mixing protocols.

Extension of this work to three dimensions and turbulent flows was done by Germaine et al. (2018), in which three scalar-field initial conditions were subjected to the action of identical (turbulent) hydrodynamic fields. Evolutions of the scalar dissipation rates in time for the three scalar fields were analyzed in a fully-developed, high-aspect-ratio turbulent channel flow via DNS. It was found that the evolution of the scalar dissipation rate (a small-scale quantity) for the three different scalar fields was dependent upon the initial geometries (a large-scale condition) of the scalar fields. Furthermore, they observed the persistence of anisotropy in the fractional components of the scalar dissipation rates for the three initial conditions.

This topic of optimal mixing conditions has been covered by many authors for different flow conditions. Foures et al. (2014) investigated optimal initial perturbations to maximize mixing of a passive scalar in a two-dimensional plane Poiseuille flow at finite Reynolds and Péclet numbers. Results from their studies showed that energy optimization led to very weak mixing of the scalar field, while optimal mixing initial perturbations homogenized the scalar field effectively. The authors also concluded that minimizing the mix-norm was able to identify optimal initial perturbations that led to effective mixing.

The work of Foures et al. (2014) was built upon by Vermach and Caulfield (2018) in their study of optimal mixing in three-dimensional plane Poiseuille flow at high Péclet numbers. The target of their study was the identification of the optimal initial velocity-field perturbation that maximized mixing by a given time horizon. They reported their findings at two different Reynolds numbers (i.e., $Re = 500$ and $Re = 3000$) and stated that the optimal perturbations that minimize the mix-norm for short time horizons result in better scalar-field mixing than optimal perturbations that minimize the scalar variance. Furthermore, the authors found that the higher Reynolds mixed scalar fields to a greater extent than the lower Reynolds number.

Minimization of the mix-norm was further explored in the work of Eggl and Schmid (2020), who proposed the use of a gradient-based nonlinear optimization scheme to improve the mixing efficiency of binary fluids by moving stirrers. Two cylindrical stirrers moving on concentric circular paths were used with an iterative direct-adjoint algorithm to enhance the mixing. Based on the findings from the simulations, the optimal stirring strategy for enhanced mixing of the binary fluids involved a combination of various mixing techniques, including plunging, unsteady vortex shedding, collisions between vortices and the wall and obstruction by the stirrers.

In the work of Eggl and Schmid (2020), the stirrers' shapes were held constant and not subjected to optimization for enhanced mixing. To address this additional optimization parameter, the work of Eggl and Schmid (2022) investigated the optimal cross-sectional shape of the stirrers in addition to the mixing strategy to further enhance scalar mixing. The authors studied four cases in their study: (i) a base configuration that was used to compare all subsequent optimizations, (ii) optimization of the cross-sectional shape of the stirrers, (iii) optimization of the velocities of the stirrers, and (iv) combined optimization of the cross-sectional shape and velocities of the stirrers. The combined optimization of the shape and the velocity of the stirrers led to the best mixing (i.e., lowest measured mix-norm) of the binary fluids. The best mixing strategy utilized processes that increased the presence of thin filaments in the scalar and of the shearing structures.

Optimal stirring by way of adaptive flow reorientation was studied by Lensvelt et al. (2022), who developed a flow-control strategy to rapidly heat a cold fluid via a hot boundary. Their research indicated that adaptive flow reorientation significantly accelerated the heating of the fluid as compared to conventional periodic schemes in terms of consistency and effectiveness. The accelerated heating was achieved by the controller via thermal plumes that extended from the heated wall into the colder fluid interior. The thermal plumes were driven by two alternating and counter-rotating circulations.

The mix-norm (Mathew et al., 2005) has been extensively used in works pertaining to mixing. Mathematically, the mix-norm is a Sobolev norm (H^q) with $q = -1/2$, and as such quantifies

the mixing process with regards to the ergodic theory. It was later shown by Lin et al. (2011) that all Sobolev norms with $q < 0$ capture mixing in the same sense as the mix-norm (i.e., in the sense of ergodic theory). Thus, Thiffeault (2012) extended the terminology of the mix-norm (Mathew et al., 2005) to encompass any negative Sobolev norm. Thiffeault further showed that the connection between negative Sobolev norms (i.e., mix-norms) and mixing exists via the property of weak convergence.

The aforementioned works suggest that there exists a dependence of the scalar mixing process on the initial scalar-field geometries. However, further investigation is required into the mechanisms that lead to the different evolutions of the mixing measures and the scalar dissipation rates for different initial conditions. Furthering our understanding of these relationships will allow for better prediction and control of flows in which scalar mixing occurs.

3 NUMERICAL METHODS

To further our understanding of the turbulent scalar mixing process, the mechanisms responsible for the mixing require further investigation. Specifically, analysis of the physical mechanisms that underlie the scalar mixing process will benefit from the calculation of the various terms in both the scalar variance budget (equation 5) and the scalar dissipation rate budget (equation 6). Several of these terms require instantaneous values of the hydrodynamic (velocity) field and the scalar (temperature) field, which must be considered at identical spatial and temporal coordinates.

While experimental methods can be used to measure and calculate some of these quantities, it becomes quite complex to simultaneously measure three components of velocity and the scalar in a volume with high spatial and temporal resolutions (Beaulac and Mydlarski, 2004b; Berajeklian and Mydlarski, 2011; Hewes and Mydlarski, 2021, 2022). The challenges posed by these requirements can be addressed via the use of direct numerical simulations. DNSs, when properly undertaken, computationally resolve all scales of the flow (i.e., the largest through to the smallest) without relying on the use of turbulence models. Alternative computational methods, such as large-eddy and Reynolds-averaged Navier-Stokes simulations rely on modeling turbulence at various scales and do not resolve the entire range of scales present in the flow. Naturally, the use of DNSs comes at a higher computational cost than the other alternatives, as more computations are involved in the resolution of the unresolved scales of the other approaches.

The work to be undertaken herein consists of first computing the hydrodynamic (velocity) field using a spectral approach that solves the continuity and momentum equations. The resulting velocity field is then used as an input to a flux-integral method solver of the advection-diffusion equation to calculate the temperature field. More details on the computations are given in the following four subsections, which describe the discretizations of the hydrodynamic-field, scalar-field, the initial and boundary conditions of the two DNSs, and the Compute Canada cluster that was used to run the simulations.

3.1 Direct Numerical Simulation of a Turbulent Channel Flow

The turbulent velocity field is calculated via DNS using a publically available code entitled CHANNELFLOW (Gibson et al., 2008; Gibson, 2010). CHANNELFLOW is a spectral solver for the three-dimensional continuity and Navier-Stokes equations, assuming constant properties on a periodic, wall-bounded domain.

3.1.1 Spatial Discretization of the Hydrodynamic Field

CHANNELFLOW uses a spectral discretization in space (Fourier \times Chebyshev \times Fourier), and finite-differencing in time (third-order semi-implicit backwards differentiation) for the velocity field. The use of spectral methods provides high accuracy and kinetic energy conserving properties, making them desirable in DNSs. The variables used to simulate the incompressible Navier-Stokes equations are the three-dimensional velocity and pressure.

The use of Fourier discretization in the streamwise (x) and spanwise (z) directions corresponds to homogeneity in these respective directions. Chebyshev polynomials are used in the wall-normal (y) direction due to the inhomogenous nature of the velocity field in this direction. (Recall that $\langle U \rangle = \langle U \rangle(y)$.) Furthermore, Chebyshev expansions allow for non-uniform spacing along the wall-normal direction, with increasing density of points as the wall is approached. The greater density of points near the wall allows for accurate resolution of the velocity in this region, where the velocity gradient is steep.

Mathematically, the velocity vector at a given spatial coordinate, $\mathbf{x} = \{x, y, z\}$, can be written in terms of its Fourier and Chebyshev expansions in the form

$$\bar{\mathbf{u}}(\mathbf{x}) = \sum_{k_x=-N_x/2+1}^{N_x/2} \sum_{n_y=0}^{N_y-1} \sum_{k_z=-N_z/2+1}^{N_z/2} \hat{\tilde{\mathbf{u}}}_{k_x, n_y, k_z} T_{n_y}(y) e^{2\pi i(k_x x/L_x + k_z z/L_z)},$$

where $(N_x \times N_y \times N_z)$ is the resolution of the simulation, $\hat{\tilde{\mathbf{u}}}$ are the spectral coefficients of the velocity field, T_m is the m^{th} Chebyshev polynomial, and $[L_x \times L_y \times L_z]$ is the size of the channel domain. The tilde and hat notations above the velocity variable denote expansions in the Fourier

and Chebyshev domains, respectively. The overbar denotes a CHANNELFLOW specific variable.

Next, the instantaneous value for the velocity field is decomposed into a base and a fluctuating component, such that:

$$\bar{\mathbf{u}}_{\text{tot}}(\mathbf{x}, t) = \bar{U}(y)\mathbf{e}_x + \bar{\mathbf{u}}(\mathbf{x}, t),$$

where \mathbf{e}_x is a unit vector along the streamwise (x) direction. Note that this decomposition is not a Reynolds decomposition in the sense that the base profile, $U(y)$, is not the mean velocity profile, and $\bar{\mathbf{u}}$ is not a turbulent fluctuation, but rather a fluctuation about the base profile. Similarly, the pressure field can also be decomposed into base and fluctuating components:

$$\bar{p}_{\text{tot}}(\mathbf{x}, t) = \Pi_x(t)x + \bar{p}(\mathbf{x}, t),$$

where Π_x is defined to be the mean pressure gradient (i.e., $d\bar{P}/dx$). The pressure gradient can also then be written in a similar manner with the following decomposition:

$$\nabla \bar{p}_{\text{tot}}(\mathbf{x}, t) = \Pi_x(t)\mathbf{e}_x + \nabla \bar{p}(\mathbf{x}, t).$$

The different forms for the base velocity and pressure components can be used in CHANNELFLOW to represent different cases such as Poiseuille, Couette, and turbulent mean profiles (Gibson, 2010). Using these decompositions and substituting them into the equations of conservation of mass and momentum, we can rewrite them in the format:

$$\nabla \cdot \bar{\mathbf{u}}_{\text{tot}} = 0, \text{ and} \tag{9}$$

$$\frac{\partial \bar{\mathbf{u}}}{\partial t} + \nabla \bar{p} = \underbrace{\nu \nabla^2 \bar{\mathbf{u}}}_{\mathbf{L}\bar{\mathbf{u}}} - \underbrace{\bar{\mathbf{u}}_{\text{tot}} \cdot \nabla \bar{\mathbf{u}}_{\text{tot}}}_{\mathbf{N}(\bar{\mathbf{u}})} + \underbrace{\left[\nu \frac{\partial^2 U}{\partial y^2} - \Pi_x \right]}_{\mathbf{C}} \mathbf{e}_x. \tag{10}$$

When written in this format, special attention must be paid to $\mathbf{N}(\bar{\mathbf{u}})$, the non-linear term ($\bar{\mathbf{u}}_{\text{tot}} \cdot \nabla \bar{\mathbf{u}}_{\text{tot}}$)

in the Navier-Stokes equation. This term can be written in several forms, which although equivalent in continuous mathematics, have different properties once discretized. The different expressions for this term are the:

$$\begin{aligned}
\text{convective form:} & \quad \bar{\mathbf{u}}_{\text{tot}} \cdot \nabla \bar{\mathbf{u}}_{\text{tot}}, \\
\text{divergence form:} & \quad \nabla \cdot (\bar{\mathbf{u}}_{\text{tot}} \bar{\mathbf{u}}_{\text{tot}}), \\
\text{skew-symmetric form:} & \quad \frac{1}{2} \bar{\mathbf{u}}_{\text{tot}} \cdot \nabla \bar{\mathbf{u}}_{\text{tot}} + \frac{1}{2} \nabla \cdot (\bar{\mathbf{u}}_{\text{tot}} \bar{\mathbf{u}}_{\text{tot}}), \text{ and} \\
\text{rotational form:} & \quad (\nabla \times \bar{\mathbf{u}}_{\text{tot}}) \times \bar{\mathbf{u}}_{\text{tot}} + \frac{1}{2} \nabla (\bar{\mathbf{u}}_{\text{tot}} \cdot \bar{\mathbf{u}}_{\text{tot}}).
\end{aligned}$$

The ideal Navier-Stokes equations preserve both linear momentum and kinetic energy. Discretization of the non-linear term using the convective form, however, results in neither of these quantities being conserved, while using the divergence form only conserves linear momentum (Zang, 1991). This then leaves the skew-symmetric and rotational forms as the only valid forms of discretization to conserve both properties. When discretized, the rotational form of the non-linear term is the least computationally expensive, but comes at the cost of introducing aliasing errors at high wavenumbers. Aliasing errors can lead to numerical instabilities and/or a decay of turbulent kinetic energy in the simulation. Therefore, the use of the rotational form requires dealiasing at high wavenumbers. The skew-symmetric form, although roughly twice as computationally expensive as the rotational form, does not lead to any aliasing errors at high wavenumbers. The difference in computational costs stems from the observation that, in general, only six derivatives are required to be calculated in the rotational form using collocation approximations, whereas 18 derivatives are required for the skew-symmetric form (Zang, 1991). It is therefore recommended to use either the rotational form with dealiasing, or the skew-symmetric form without dealiasing. For the present work, the skew-symmetric form was used without dealiasing.

Defining a modified pressure, \bar{q} , such that:

$$\bar{q} = \begin{cases} \bar{p} + \frac{1}{2} \bar{\mathbf{u}} \cdot \bar{\mathbf{u}} & \text{if } \mathbf{N}(\bar{\mathbf{u}}) = \text{Rotational} \\ \bar{p} & \text{else} \end{cases}$$

and rearranging equation (10) with the linear ($\mathbf{L}\bar{\mathbf{u}}$), non-linear ($\mathbf{N}(\bar{\mathbf{u}})$), and constant (in-space) term (\mathbf{C}), we can write:

$$\frac{\partial \bar{\mathbf{u}}}{\partial t} + \nabla \bar{q} = \mathbf{L}\bar{\mathbf{u}} - \mathbf{N}(\bar{\mathbf{u}}) + \mathbf{C}.$$

The last step in deriving the Fourier-transformed version of equation (10) is to define the Fourier-transformed operators for the gradient, Laplacian, and the linear operator \mathbf{L} , so that

$$\begin{aligned} \tilde{\nabla}_{k_x k_z} &\triangleq 2\pi i \frac{k_x}{L_x} \mathbf{e}_x + \frac{\partial}{\partial y} \mathbf{e}_y + 2\pi i \frac{k_z}{L_z} \mathbf{e}_z, \\ \tilde{\nabla}_{k_x k_z}^2 &\triangleq \frac{\partial^2}{\partial y^2} - 4\pi^2 \left(\frac{k_x^2}{L_x^2} + \frac{k_z^2}{L_z^2} \right), \\ \tilde{\mathbf{L}}_{k_x k_z} &\triangleq \nu \tilde{\nabla}_{k_x k_z}^2. \end{aligned}$$

Further noting that $\widetilde{\nabla \bar{q}} = \tilde{\nabla} \tilde{\bar{q}}$, and that $\widetilde{\mathbf{L}\bar{\mathbf{u}}} = \tilde{\mathbf{L}}\tilde{\bar{\mathbf{u}}}$ (due to the linearity of the operator), and dropping the $k_x k_z$ subscript for convenience, one can write the Fourier-transformed versions of equations (9) and (10) as:

$$\tilde{\nabla} \cdot \tilde{\bar{\mathbf{u}}} = 0, \text{ and} \tag{11}$$

$$\frac{\partial \tilde{\bar{\mathbf{u}}}}{\partial t} + \tilde{\nabla} \tilde{\bar{q}} = \tilde{\mathbf{L}}\tilde{\bar{\mathbf{u}}} - \widetilde{\mathbf{N}(\bar{\mathbf{u}})} + \tilde{\mathbf{C}}. \tag{12}$$

Equations (11) and (12) are thus the continuity and Navier-Stokes equations written in spectral form. Since CHANNELFLOW is a spectral solver, the formulations of the equations are carried out in the spectral domain. The use of Fourier and Chebyshev transformations make it convenient to convert the velocity and pressure fields back and forth between the physical and spectral formulations.

3.1.2 Temporal Discretization of the Hydrodynamic Field

CHANNELFLOW offers the user a variety of time-stepping algorithms that are suitable and optimal under different conditions. In general, the simplest formulation that is also convenient for writing a generalized form of the time-stepping algorithm is the second-order Crank-Nicholson/Adams-Bashforth (CNAB) mixed time-stepping scheme. This scheme treats the non-linear term, $\mathbf{N}(\bar{\mathbf{u}})$, explicitly and the linear term, $\mathbf{L}\bar{\mathbf{u}}$, implicitly (Gibson, 2010).

If we write the approximation of $\tilde{\mathbf{u}}$ at time $t = n\Delta t$ as $\tilde{\mathbf{u}}^n$, and define the non-linear term as $\tilde{\mathbf{N}}^n \triangleq \widetilde{\mathbf{N}(\bar{\mathbf{u}})}$, then the terms in equation (12) can be discretized temporally at time $t = (n-1/2)\Delta t$ as follows (Gibson, 2010):

$$\begin{aligned}\frac{\partial}{\partial t} \tilde{\mathbf{u}}^{n+1/2} &= \frac{\tilde{\mathbf{u}}^{n+1} - \tilde{\mathbf{u}}^n}{\Delta t} + O(\Delta t^2) \\ \tilde{\mathbf{L}}\tilde{\mathbf{u}}^{n+1/2} &= \frac{1}{2}\tilde{\mathbf{L}}\tilde{\mathbf{u}}^{n+1} + \frac{1}{2}\tilde{\mathbf{L}}\tilde{\mathbf{u}}^n + O(\Delta t^2) \\ \tilde{\nabla}\tilde{q}^{n+1/2} &= \frac{1}{2}\tilde{\nabla}\tilde{q}^{n+1} + \frac{1}{2}\tilde{\nabla}\tilde{q}^n + O(\Delta t^2) \\ \tilde{\mathbf{N}}^{n+1/2} &= \frac{3}{2}\tilde{\mathbf{N}}^n - \frac{1}{2}\tilde{\mathbf{N}}^{n-1} + O(\Delta t^2) \\ \tilde{\mathbf{C}}^{n+1/2} &= \frac{1}{2}\tilde{\mathbf{C}}^{n+1} + \frac{1}{2}\tilde{\mathbf{C}}^n + O(\Delta t^2).\end{aligned}$$

The naming convention for the CNAB time-stepping algorithm originates from the observation that the linear term approximation is called Crank-Nicholson and the approximation for the non-linear term is called Adams-Bashforth (Canuto et al., 1988). These expansions can be applied to equation (12) while accounting for time-stepping schemes that may also involve substepping in time (e.g., Runge-Kutta schemes), and thus deriving a generalized formulation written as:

$$\nu \tilde{\mathbf{u}}^{n,i+1} - \lambda \tilde{\mathbf{u}}^{n,i+1} - \tilde{\nabla}\tilde{q}^{n,i+1} = -\tilde{\mathbf{R}}^{n,i},$$

where:

$$\begin{aligned}\lambda &\triangleq \frac{1}{\beta_i \Delta t} + 4\pi^2 \nu \left(\frac{k_x^2}{L_x^2} + \frac{k_z^2}{L_z^2} \right) \\ \tilde{\mathbf{u}}'' &\triangleq \frac{\partial^2}{\partial y^2} \tilde{\mathbf{u}} \\ \tilde{\mathbf{R}}^{n,i} &\triangleq \left[\frac{1}{\beta_i \Delta t} + \frac{\alpha_i \tilde{\mathbf{L}}}{\beta_i} \right] \tilde{\mathbf{u}}^{n,i} + \frac{\alpha_i}{\beta_i} \tilde{\nabla} \tilde{q}^{n,i} + \frac{\gamma_i}{\beta_i} \tilde{\mathbf{N}}^{n,i} + \frac{\zeta_i}{\beta_i} \tilde{\mathbf{N}}^{n,i-1} + \tilde{\mathbf{C}}^{n,i+1} + \frac{\alpha_i}{\beta_i} \tilde{\mathbf{C}}^{n,i}.\end{aligned}$$

Note that the n superscript denotes the time-step and the i superscript denotes the sub-step where applicable. Furthermore, α , β , γ , and ζ are coefficients that vary based on the time-stepping scheme that is being used for discretization in the temporal domain. Combining this formulation along with the continuity equation gives us the system of equations to be solved as:

$$\begin{aligned}\tilde{\nabla} \cdot \tilde{\mathbf{u}} &= 0 \\ \nu \tilde{\mathbf{u}} - \lambda \tilde{\mathbf{u}} - \tilde{\nabla} \tilde{q} &= -\tilde{\mathbf{R}}\end{aligned}$$

Therefore, CHANNELFLOW simulates a turbulent channel flow by solving/advancing these equations as a coupled system within the specified domain along with the user-specified boundary conditions by looping over the Fourier modes. The approach used for solving this system of equations is the influence-matrix method, where the system of equations is rearranged into an influence-matrix equation using the specified boundary conditions.

3.2 Direct Numerical Simulation of Passive Scalar Transport

Once the hydrodynamic field has been computed, it is then used as input to solve the advection-diffusion equation using a code entitled 3DFLUX. 3DFLUX (Germaine et al., 2013) is a fully three-dimensional, high-order, conservative, flux integral method for solving the scalar transport equation. Recall that the study of a passive scalar implies that the hydrodynamic field is dynamically independent of the scalar field, even though the latter is advected and diffused by the former. Thus, the velocity field is computed using CHANNELFLOW, and the scalar field is calculated

using 3DFLUX, the implementation of which is discussed in the following subsection.

The use of spectral methods, as in the case of the velocity field, is not well-suited to the solution of the advection-diffusion equation due to the presence of sharp gradients in the scalar field (such as a rapid change in scalar concentration across an interface, as used in this work), which lead to a decay of the convergence rate of such spectral schemes due to the Gibbs phenomenon (Germaine et al., 2013). Furthermore, certain scalar fields may not be periodic in the streamwise direction (even though the velocity field is). Thus, the use of spectral methods for solving non-periodic problems such as the scalar fields considered in this work is not very attractive (Simens et al., 2009). The remaining subsections give an overview of the spatial and temporal discretizations of the scalar-field as used in 3DFLUX. For more details on 3DFLUX, the reader is referred to Germaine et al. (2013).

3.2.1 Spatial Discretization of the Scalar Transport Equation

Spatial discretization of the scalar field is done via the use of non-overlapping control volumes of size $\Delta V = \Delta x \times \Delta y \times \Delta z$, with corresponding grid nodes placed at the center of these cells (Germaine et al., 2013). An average value of the scalar quantity, $\tilde{\theta}$, within a control volume, ΔV , is assigned to the grid node at the center of each cell, and hereby denoted via ϕ . The velocity components of the imported hydrodynamic field (u , v , and w) are stored at the centers of the cell faces in a staggered formation. This arrangement ensures that the velocity components are readily available at the cell-sides to calculate the fluxes exchanged between adjacent cells.

Special care must be taken when transforming the hydrodynamic field from a spectral representation (i.e., CHANNELFLOW) to a finite-volume representation (i.e., 3DFLUX). As noted above, 3DFLUX requires the velocity components to be defined at the cell faces in a staggered grid arrangement, and the velocity field must be interpolated to achieve this requirement. The velocity field is interpolated to the new grid size via spectral (exact) interpolation. However, this interpolation induces an artificial divergence to the velocity field, such that a very small-correction (less than 0.01%) is applied to the streamwise (u) component of the velocity field to guarantee the

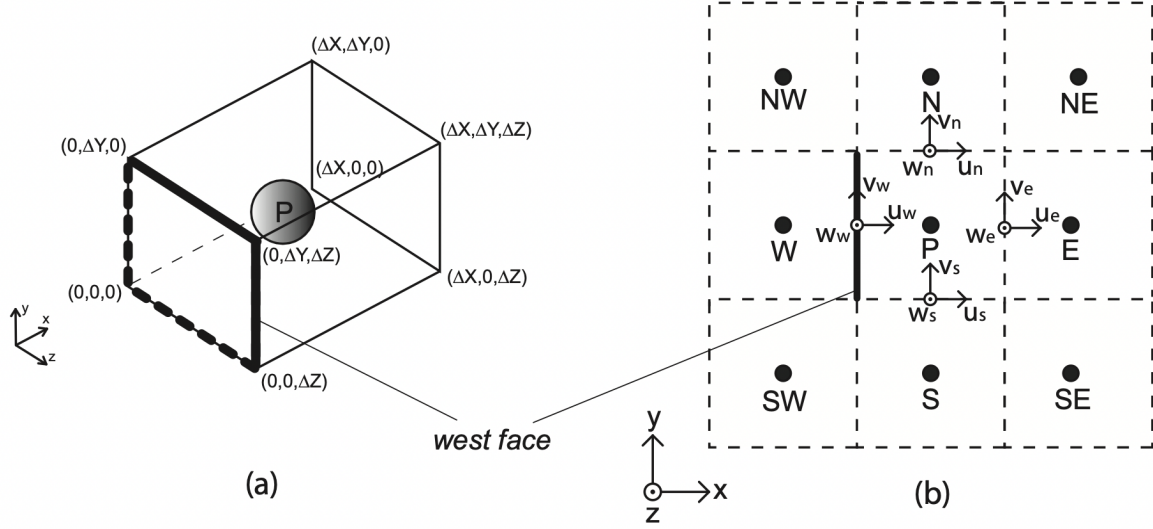


Figure 2: Spatial discretization of the scalar transport equation (taken from Germaine et al. (2013)).

divergence-free condition as required by the conservation of mass restraint (Germaine et al., 2014).

To make the study and analysis of this finite volume method more convenient, nomenclature (Patankar, 1980) is introduced. The grid node located at the center of each volume is assigned the letter P . Relative to P , we assign the letters N, S, E, W, B , and F represent nodes to the north, south, east, west, back, and front of the referenced cell. Note that the capital letters can also be combined to denote cells in diagonal directions to P (e.g., SW denotes a grid node located at the center of a computational cell that is in the negative x and negative y directions relative to the cell containing P). Visualization of this discretization is depicted in figure 2, along with the placements of the velocity components on the cell faces. Furthermore, lower-case letters are used as subscripts to refer to quantities in the directions referenced by the noted letters (e.g., U_w).

Having described the spatial notation, one may rewrite the integral form of the advection-diffusion equation as follows (Germaine et al., 2013):

$$\underbrace{\int_{\Delta t} \int_{\Delta V} \frac{\partial \phi}{\partial t} dV dt}_{(i)} = \int_{\Delta t} \int_{\Delta V} \left[\underbrace{-\nabla \cdot (\mathbf{u}\phi)}_{(ii)} + \underbrace{\nabla \cdot (\alpha \nabla \phi)}_{(iii)} + \underbrace{S}_{(iv)} \right] dV dt. \quad (13)$$

Term (i) can be discretized as follows:

$$\int_{\Delta t} \int_{\Delta V} \frac{\partial \phi}{\partial t} dV dt = (\phi^{t+\Delta t} - \phi^t) \Delta V$$

since the value of the scalar at the node P is the average value of the scalar within the control volume. Term (ii) can be rearranged as follows:

$$\begin{aligned} \int_{\Delta t} \int_{\Delta V} -\nabla \cdot (\mathbf{u}\phi) dV dt &= \Delta y \Delta z \int_{\Delta t} (u_w \phi_w - u_e \phi_e) dt \\ &+ \Delta x \Delta z \int_{\Delta t} (v_s \phi_s - v_n \phi_n) dt \\ &+ \Delta x \Delta y \int_{\Delta t} (w_b \phi_b - w_f \phi_f) dt. \end{aligned}$$

Note that the terms on the right hand side of this equation (i.e., the advective terms) can be rewritten using an averaging scheme, e.g.,:

$$\Delta y \Delta z \int_{\Delta t} (u_w \phi_w) dt = \langle u_w \phi_w \rangle \Delta y \Delta z \Delta t,$$

where $\langle \cdot \rangle$ represents temporal averaging over the time interval Δt . Rearrangement of term (iii) is done as follows:

$$\begin{aligned} \int_{\Delta t} \int_{\Delta V} \nabla \cdot (\alpha \nabla \phi) dV dt &= \Delta y \Delta z \int_{\Delta t} \alpha \left(\frac{\partial \phi}{\partial x} \Big|_e - \frac{\partial \phi}{\partial x} \Big|_w \right) dt \\ &+ \Delta x \Delta z \int_{\Delta t} \alpha \left(\frac{\partial \phi}{\partial y} \Big|_n - \frac{\partial \phi}{\partial y} \Big|_s \right) dt \\ &+ \Delta x \Delta y \int_{\Delta t} \alpha \left(\frac{\partial \phi}{\partial z} \Big|_f - \frac{\partial \phi}{\partial z} \Big|_b \right) dt. \end{aligned}$$

The terms on the right hand side of this equation (i.e., the diffusive terms) can also be rewritten using the introduced averaging:

$$\Delta y \Delta z \int_{\Delta t} -\alpha \frac{\partial \phi}{\partial x} \Big|_w dt = \left\langle -\alpha \frac{\partial \phi}{\partial x} \Big|_w \right\rangle \Delta y \Delta z \Delta t.$$

Lastly, the source term (iv) can be written:

$$\int_{\Delta t} \int_{\Delta V} S \, dV dt = \langle S \rangle \Delta t \Delta V.$$

Using these averaged representations, equation (13) can be written as the sum of various flux terms, such that:

$$\phi^{t+\Delta t} = \phi_P^t + \mathbf{f}_w - \mathbf{f}_e + \mathbf{f}_s - \mathbf{f}_n + \mathbf{f}_b - \mathbf{f}_f + \langle S \rangle \Delta t. \quad (14)$$

The six flux terms, \mathbf{f}_w , \mathbf{f}_e , \mathbf{f}_s , \mathbf{f}_n , \mathbf{f}_b , and \mathbf{f}_f represent the sum of the advective and diffusive fluxes across the faces relative to the node P , as indicated by the subscripts. The flux terms across the west, south, and back faces relative to P are defined as:

$$\begin{aligned} \mathbf{f}_w &= \frac{\Delta t \Delta y \Delta z}{\Delta V} \left(\langle u_w \phi_w \rangle - \left\langle \alpha \frac{\partial \phi}{\partial x} \Big|_w \right\rangle \right) \\ \mathbf{f}_s &= \frac{\Delta t \Delta x \Delta z}{\Delta V} \left(\langle u_s \phi_s \rangle - \left\langle \alpha \frac{\partial \phi}{\partial y} \Big|_s \right\rangle \right) \\ \mathbf{f}_b &= \frac{\Delta t \Delta x \Delta y}{\Delta V} \left(\langle u_b \phi_b \rangle - \left\langle \alpha \frac{\partial \phi}{\partial z} \Big|_b \right\rangle \right). \end{aligned}$$

Due to the conservative nature of this formulation, the flux across adjacent cells will be identical. Thus, the calculation of the west, south, and back faces of a given cell is sufficient to resolve the flux through the volume. The remaining fluxes, i.e., fluxes through the east, north, and front faces can be computed using the already calculated fluxes, such that:

$$(\mathbf{f}_e)_{i,j,k} = (\mathbf{f}_w)_{i+1,j,k}$$

$$(\mathbf{f}_n)_{i,j,k} = (\mathbf{f}_s)_{i,j+1,k}$$

$$(\mathbf{f}_f)_{i,j,k} = (\mathbf{f}_b)_{i,j,k+1}.$$

It should be noted that the values of ϕ and its gradients are required at the cell faces to compute the advective and diffusive fluxes across adjacent cells. Since ϕ is stored at cell centers rather than at the cell faces, ϕ and its gradients are interpolated from the known values at the cell-centered

nodes. A quadratic polynomial is used to interpolate the scalar, $\phi(x, y, z)$, at each time step, where the interpolant, ψ , is defined as:

$$\psi(x, y, z) = \sum_{i=0}^2 \sum_{j=0}^2 \sum_{k=0}^2 c_{ijk} x^i y^j z^k, \quad (15)$$

where c_{ijk} represent ten unknown coefficients. The unknown coefficients are computed by subjecting the interpolation to the constraint that the average value of the interpolant, ψ , and its derivatives be equal to the average value of the scalar and its derivatives stored at the cell centers.

3.2.2 Temporal Discretization of the Scalar Transport Equation

Whereas the spatial discretization of the scalar transport equation is done in an Eulerian frame of reference, the temporal discretization of the equation is done using a Lagrangian one. The use of a semi-Lagrangian approach allows for larger time steps than classical Eulerians schemes and also ensures better stability (Germaine et al., 2013). The time-averaged sum of the advective and diffusive fluxes across the west face (used as an example from hereon) over a time interval Δt can be written in the form:

$$\langle u_w \phi_w \rangle - \left\langle \alpha \frac{\partial \phi}{\partial x} \Big|_w \right\rangle = \frac{1}{\Delta t} \int_0^{\Delta t} u_w \phi_w - \alpha \frac{\partial \phi}{\partial x} \Big|_w dt.$$

The advective and diffusive fluxes across the west face of the cell represent the amount of the scalar that is transported across that face, and is an average of the scalar properties over the volume of fluid that is transported into the cell through the face within the time interval Δt .

Continuing to use the west face of the cell as an example, the amount of fluid that crosses through this face into the cell over a time interval Δt is given by $\Delta V_p = u_w \Delta t \times \Delta y \times \Delta z$. This volume is approximated using a rectangular prism, which is transported into the cell, P , and represents contributions of fluid particles that originate in the neighboring cells of P . Although the vertices of the rectangular prism are aligned with the vertices of the west face of the cell after the time interval, Δt , the coordinates of the vertices at the originating location of the fluid volume can

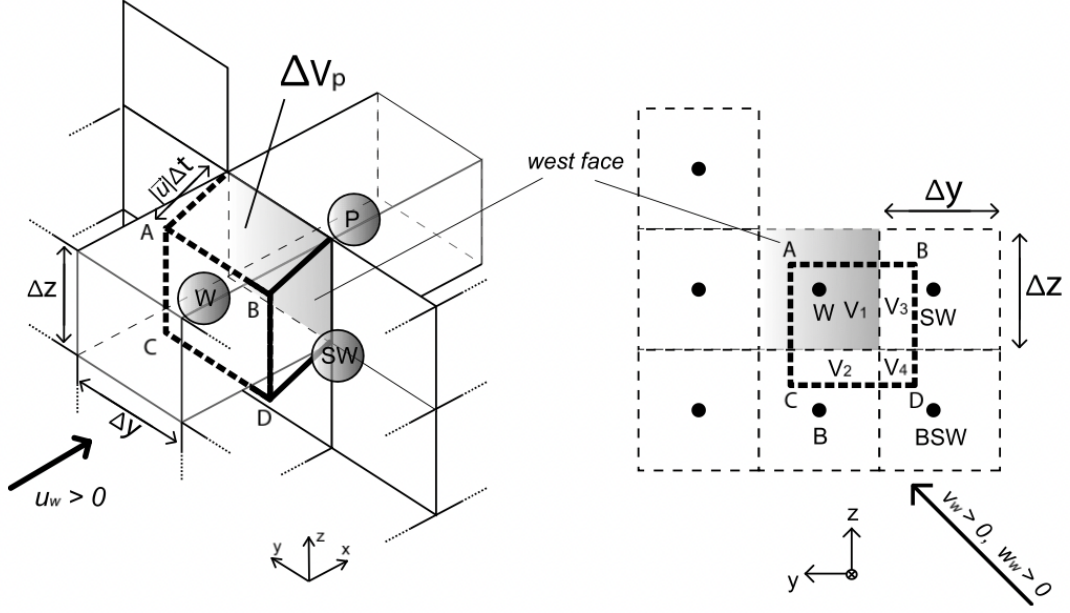


Figure 3: Transport of the fluid volume, ΔV_p , over the time interval Δt (taken from Germaine et al. (2013)).

be found by integrating the equation of a fluid particle located at $\mathbf{x}(x, y, z)$:

$$\frac{d\mathbf{u}}{dt} = \mathbf{u}(\mathbf{x}, t),$$

backward in time over a time interval Δt . Since the locations of the vertices after the time interval are known, the set of equations identifying the coordinates of the vertices A, B, C, and D can be formulated as follows:

$$\begin{cases} x(0) = \Delta x - u_w \Delta t \\ y(0) = \Delta y - v_w \Delta t = \Delta y + v_w \frac{x(0) - \Delta x}{u_w} \\ z(0) = \Delta z - w_w \Delta t = \Delta z + w_w \frac{x(0) - \Delta x}{u_w}. \end{cases}$$

Now integrating the scalar quantity over the rectangular prism that crosses over into the cell volume and using the interpolants ψ (introduced in section 3.2.1), we can formulate an equation for the

time-averaged advective fluxes over the interval Δt as:

$$\begin{aligned} \langle u_w \phi_w \rangle = & \frac{1}{\Delta t \Delta y \Delta z} \times \left\{ \int_0^{z(0)} \int_0^{y(0)} \left[\int_{x(0)}^{\Delta x} \psi_W dx + u_w \frac{\Delta t^2}{2} (\nabla \cdot (\alpha \nabla \psi_W) + S_W) \right] dy dz \right. \\ & + \int_0^{z(0)} \int_{y(0)}^{\Delta y} \left[\int_{x(0)}^{\Delta x} \psi_B dx + u_w \frac{\Delta t^2}{2} (\nabla \cdot (\alpha \nabla \psi_B) + S_B) \right] dy dz \\ & + \int_{z(0)}^{\Delta z} \int_{y(0)}^{\Delta y} \left[\int_{x(0)}^{\Delta x} \psi_{BSW} dx + u_w \frac{\Delta t^2}{2} (\nabla \cdot (\alpha \nabla \psi_{BSW}) + S_{BSW}) \right] dy dz \\ & \left. + \int_{z(0)}^{\Delta z} \int_0^{y(0)} \left[\int_{x(0)}^{\Delta x} \psi_{SW} dx + u_w \frac{\Delta t^2}{2} (\nabla \cdot (\alpha \nabla \psi_{SW}) + S_{SW}) \right] dy dz \right\}. \end{aligned}$$

Similarly, the time-averaged equation for the diffusive fluxes over the interval Δt is written as:

$$\begin{aligned} \left\langle \alpha \frac{\partial \phi}{\partial x} \Big|_w \right\rangle = & \frac{\alpha}{u_w \Delta t \Delta y \Delta z} \int_{x(0)}^{\Delta x} \left[\int_0^{z(0)} \int_0^{y(0)} \frac{\partial \psi}{\partial x} \Big|_W dy dz \right. \\ & + \int_0^{z(0)} \int_{y(0)}^{\Delta y} \frac{\partial \psi}{\partial x} \Big|_B dy dz \\ & + \int_{z(0)}^{\Delta z} \int_0^{y(0)} \frac{\partial \psi}{\partial x} \Big|_{SW} dy dz \\ & \left. + \int_{z(0)}^{\Delta z} \int_{y(0)}^{\Delta y} \frac{\partial \psi}{\partial x} \Big|_{BSW} dy dz \right] dx. \end{aligned}$$

The two equations presented for the time-averaged advective and diffusive fluxes can be extended to other faces of the cell volume similarly. Additionally, it should be noted that these equations assume that the source term, S , is constant within a given cell for the duration of Δt , and that the properties of the fluid are constant.

3.3 Boundary & Initial Conditions

The DNS of the velocity field is computed using no-penetration / no-slip boundary conditions imposed at the walls of the channel ($y = 0$ and $y = 2h$, where h is the half-height of the channel), and periodic boundary conditions in the streamwise (x) and spanwise (z) directions. Simulation of the hydrodynamic field is conducted at $Re_\tau = 190$ over a domain of size $2\pi h \times 2h \times \pi h$, in

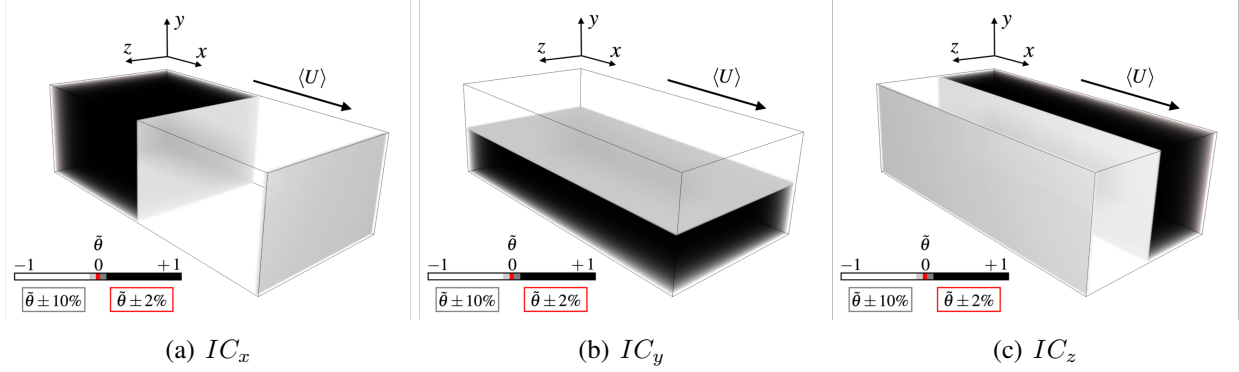


Figure 4: The three scalar-field initial conditions studied herein. (Imagery generated using VAPOR, www.vapor.ucar.edu).

the streamwise (x), wall-normal (y) and spanwise (z) directions, respectively, with a resolution of $256 \times 193 \times 192$. An initial velocity field with random, divergence-free perturbations is used to initialize the simulation. Once the velocity field has evolved such that the flow is fully turbulent (i.e., the instantaneous velocity profile becomes turbulent), the simulation is frozen at an instance in time (i.e., $t \approx 4000s$) and the given velocity field is then used as the starting velocity field (i.e., $\tau = 0$) to begin the mixing of the scalar field. Additional statistics, such as the root-mean-square (RMS) of the turbulent velocity fluctuations, are analyzed for the hydrodynamic field at $\tau = 0$ to ensure that the velocity field is indeed fully turbulent.

DNS of the scalar field is undertaken on the same domain of $2\pi h \times 2h \times \pi h$, using a uniform grid with a resolution of $514 \times 195 \times 194$ to resolve both the large and small scales of the scalar field. Adiabatic boundary conditions are imposed at the walls with periodic boundary conditions along the streamwise (x) and spanwise (z) directions.

As noted when introducing the motivation behind the work herein, the evolution of the mixing with time will be studied for three different scalar field initial conditions, IC_x , IC_y and IC_z , as depicted in figure 4. These fields consist of two equal volumes of uniform concentrations, $\tilde{\theta} = +1$ (black) and -1 (white), separated by two interfaces (due to the periodic boundary conditions in x and z) of total area $4\pi h^2 (= 2 \times 2h \times \pi h)$ for IC_x and $8\pi h^2 (= 2 \times 2h \times 2\pi h)$ for IC_z and a single interface of area $2\pi^2 h^2 (= 2\pi h \times \pi h)$ for IC_y . The transition from one region of uniform

concentration to another (i.e., from $\tilde{\theta} = +1$ to $\tilde{\theta} = -1$) follows a sinusoidal function. The scalar concentration across the interface(s) is defined by the function:

$$\tilde{\theta} = \sin\left(\frac{\pi}{2} + \frac{x_i - x_{int}}{L_{int}}\pi\right),$$

where x_i is the coordinate normal to the interface, x_{int} is the coordinate that marks the beginning of the interface, and L_{int} is the width of the interface. The width of the interface was set to be equal to approximately 10% of the channel height for all three scalar-field initial conditions, such that $L_{int} = 0.2h$. All fields have zero mean concentration. Note that all three scalar fields are subjected to identical turbulent velocity fields, and thus any changes in evolutions of the three scalar fields will be a sole result of the orientations of the initial scalar fields with respect to the velocity field. All three scalar-fields were simulated over the time interval $0 \leq \tau \leq 7$, where $\tau \equiv tu_\tau/h$.

3.4 Compute Canada Cluster

The simulations conducted herein were run on Compute Canada’s Graham cluster. The Graham cluster is a collection of 41,548 cores spread across 1,185 nodes of various types that are all connected via a low-latency high-bandwidth Infiniband fabric. CHANNELFLOW’s ability to utilize message passing interface (MPI) allowed for the hydrodynamic simulation to be run across multiple nodes using a total of 128 cores in parallel. For 3DFLUX, Intel’s Thread Building Blocks (TBB) library was used to take advantage of multithreading across 32 CPU cores located on the same node for each of the three scalar-field initial conditions. For both the velocity and scalar-field simulations, the computations were performed using Intel E5-2683 v4 Broadwell CPUs running at 2.1 GHz.

The CPU time required for the hydrodynamic field simulation was 0.12 CPU years, corresponding to a wall-clock time of 8 hours. For each of the three scalar-field simulations, the CPU time required was 1.84 CPU years, corresponding to a wall-clock time of three weeks. The hydrodynamic field simulation produced 40,000 files of 240 MB each (velocity field) and 40,000 files of

80 MB each (pressure field), for a total storage size of 12.8 TB for the CHANNELFLOW simulations. For each of the three scalar-field initial condition simulations, the output consisted of 40,000 files of 156 MB each, resulting in a total storage size of 18.72 TB across all three scalar-field initial conditions. In total, the storage requirements were 31.52 TB for the velocity, pressure, and scalar fields combined.

4 RESULTS

The presentation of the results in the following subsections is divided such that the reader is presented with *i)* a discussion regarding the averaging schemes used in the analysis, *ii)* a presentation of results validating the hydrodynamic field, and *iii)* the analysis of the scalar-field results. Discussion of the scalar-field results is further sub-divided into results corresponding to the mixing metrics, scalar variance budget, and the scalar dissipation rate budget.

4.1 Averaging Schemes

Given the complex nature of the velocity and scalar fields studied in this work, the ensuing analysis of the metrics and other statistics requires special care to treat the hydrodynamic and scalar fields meaningfully. Whereas the velocity field is statistically stationary, the scalar fields are all unsteady, as they evolve from their initial states to the mixed state. The velocity field is also inhomogeneous in the wall-normal (y -) direction. Additionally, the homogeneity of the three scalar fields are different. The scalar field resulting from the IC_x initial condition is statistically homogeneous in the z -direction (only). That resulting from the IC_y initial condition is statistically homogeneous in the x - and z -directions. Lastly, the scalar field resulting from the IC_z initial condition is statistically homogeneous in the x -direction (only).

The underlying symmetries and ensuing statistical (in-)homogeneities associated with the different initial conditions, as well as the statistical non-stationary nature of the scalar field, must be considered when analyzing the results. A primary consequence of this fact is that one can no longer simply volume-average the terms in equations 5 and 6 if one wants to examine the evolution(s) of all their constituent terms, because some of the various, relevant terms become zero when volume-averaged. Moreover, there is no “universal” approach to spatial averaging that can be employed that will not eliminate some of the pertinent terms in describing the evolutions of the scalar fields. For example, were one to average scalar-field statistics in the z -direction, certain terms in eq. (6) – such as production by the mean scalar gradient – will become zero for the IC_z

case, only, because $\partial\langle\cdot\rangle_z/\partial z = 0$ due to the statistical homogeneity in the z -direction. Because volume-averaging is no longer feasible, averaging will be taken over (spatial) planes (at specific locations within the channel) to investigate the terms in equations 5 and 6. However, because the amount of data in a plane is (much) less than in a volume, the statistical convergence of the data is reduced. To address this, local time averages will also be employed (i.e., averaging statistics in time from $\tau' = 0$ to $\tau' = \tau$), which will improve convergence of the data, while retaining its time-dependence. Moreover, certain analyses will also involve local spatial averages after having performed the time-average, which, when calculated in this way, do not eliminate terms and further aid convergence.

Having introduced the complexities and intricacies associated with the analysis of the results in this 3-D unsteady, inhomogeneous problem, the specific averaging conventions used herein will now be discussed. The simplest averaging scheme that will be used in the following subsections is volume averaging, which will be denoted by $\langle\cdot\rangle_{x,y,z} = \langle\cdot\rangle_V$. Volume-averaging is ideal for studying the scalar dissipation rate, which in this context will capture the average rate at which the scalar variance is destroyed in the channel as a function of time. When analyzing the scalar variance and scalar dissipation rate budgets, planar averaging will be used. For each of the scalar-field initial conditions, spatial averages will be taken over planes (at specific locations) that are parallel to the interface(s) separating the two initial scalar concentrations.

In the case of IC_x , averages will be taken along $y - z$ planes, such that the averaging used is denoted as $\langle\cdot\rangle = \langle\cdot\rangle_{y,z}$. This approach ensures that the terms analyzed in equations 5 and 6 for IC_x are functions of both time and space in the inhomogeneous direction (x) only. A similar approach is taken for the other two scalar fields, such that the averaging used for the IC_y initial condition is denoted by $\langle\cdot\rangle = \langle\cdot\rangle_{x,z}$ and that for the IC_z initial condition is given by $\langle\cdot\rangle = \langle\cdot\rangle_{x,y}$. Thus, for all three scalar fields, the terms in the scalar variance and scalar dissipation rate budgets (equations 5 and 6) will be functions of both time and a single spatial direction, corresponding to the direction of inhomogeneity for the respective scalar field.

To increase the convergence of the terms in the aforementioned equations, local time averaging (i.e., a running time average) is used. To this end, the temporal average defined at the time τ is taken over the time interval $0 \leq \tau' \leq \tau$. This approach is denoted in the appropriate figures using the notation:

$$\frac{1}{\tau} \int_{\tau'=0}^{\tau'=\tau} Term \, d\tau',$$

where $Term$ represents a term in the budget that has already been spatially averaged along its respective plane. Lastly, a final approach taken to improve the convergence and capture the evolution(s) of the various terms over the entire channel is to average the terms over all planes along the direction of inhomogeneity. For example, in the case of IC_x , the terms are averaged along $y - z$ planes which are normal to the x axis and will change in that direction. For optimal convergence, the averages of the terms (in the IC_x case) are calculated using all $y - z$ planes normal to the x axis along the entire length of the channel. When used, this scheme is denoted as follows:

$$\frac{1}{L} \int_{l=0}^{l=L} Term \, dl,$$

where L represents the distance represented along the direction of inhomogeneity (the channel length in this case). In certain instances, both approaches are combined, such that the final averaging scheme is given via a combination of the two aforementioned schemes, and is denoted by:

$$\frac{1}{L} \frac{1}{\tau} \int_{l=0}^{l=L} \int_{\tau'=0}^{\tau'=\tau} Term \, d\tau' dl.$$

4.2 Velocity Field

In this section, the hydrodynamic (velocity) field generated via CHANNELFLOW is *i*) presented, and *ii*) validated against published data generated via DNS for similar simulations. Validation is performed by comparing profiles of the mean longitudinal velocity and the root-mean-square (RMS) value of the three velocity components as functions of the wall-normal distance with the works of Abe et al. (2001) and Germaine et al. (2014) in figure 5.

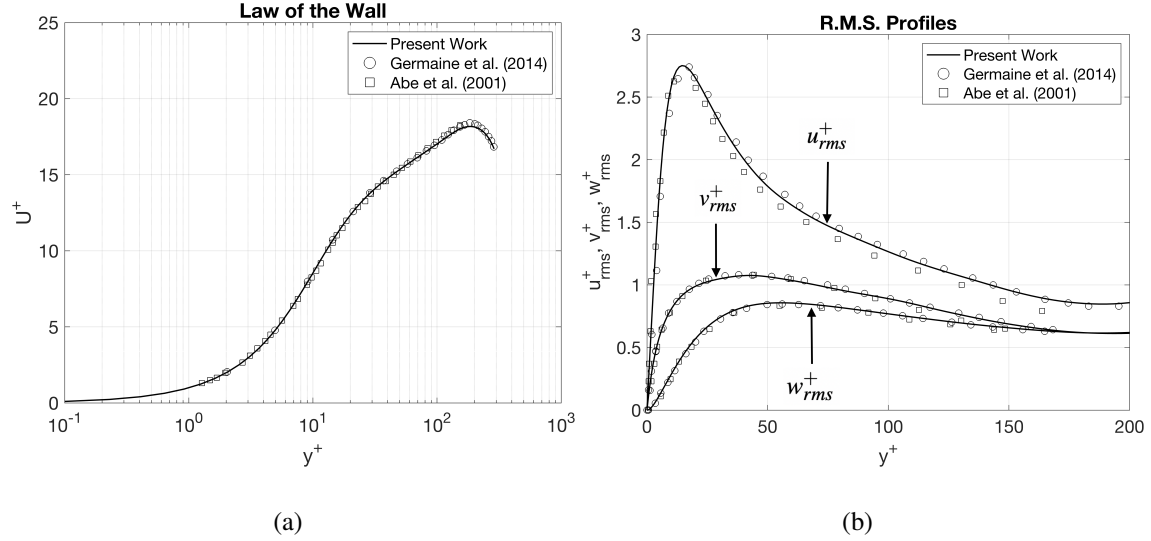


Figure 5: Mean streamwise component of the velocity field (a) and the root-mean-square (RMS) values of the three velocity field components (b) and comparisons with the work of Abe et al. (2001) and Germaine et al. (2014).

As observed in figure 5(a), the mean longitudinal velocity follows a linear profile in the viscous sublayer ($y^+ < 5$) and a logarithmic profile in the log-law region ($30 \lesssim y^+ \leq 100$). The present data agrees with established analytic profiles as well as the results of Abe et al. (2001) and Germaine et al. (2014). The RMS profiles of the three velocity components are also validated against the works of Abe et al. (2001) and Germaine et al. (2014) in figure 5(b). The peak observed in the near-wall region for the u^+_{rms} profile corresponds to peak turbulent activity in the near-wall region. Excellent agreement is observed once again between the present work and the prior published data for the RMS profiles.

4.3 Scalar Field

Evolutions of the scalar fields are analyzed by first calculating the mixing metrics and the volume-averaged scalar dissipation rate. These metrics quantify the rates at which the mixing occurs for the different scalar-field initial conditions. Next, the terms in the scalar variance budget are calculated and analyzed to better understand the balance of the scalar dissipation rate with the other physical mechanisms. Lastly, the terms in the scalar dissipation rate budget are analyzed to further our

understanding of the evolution of the scalar dissipation rate, specifically its production by various physical phenomena.

4.3.1 Mixing Metrics

The three scalar-field initial conditions visualized in figure 4 were subjected to the action of identical hydrodynamic fields over the time interval $0 \leq \tau \leq 7$. The use of identical velocity fields for advecting and diffusing all three scalar-field initial conditions ensures that any differences observed in the evolutions of these fields will be a sole result of the orientation of the initial scalar field. Plotted in figure 6 are the scalar field distributions that result from the action of the turbulent channel flow on the scalar-field initial conditions at time $\tau = 7$.

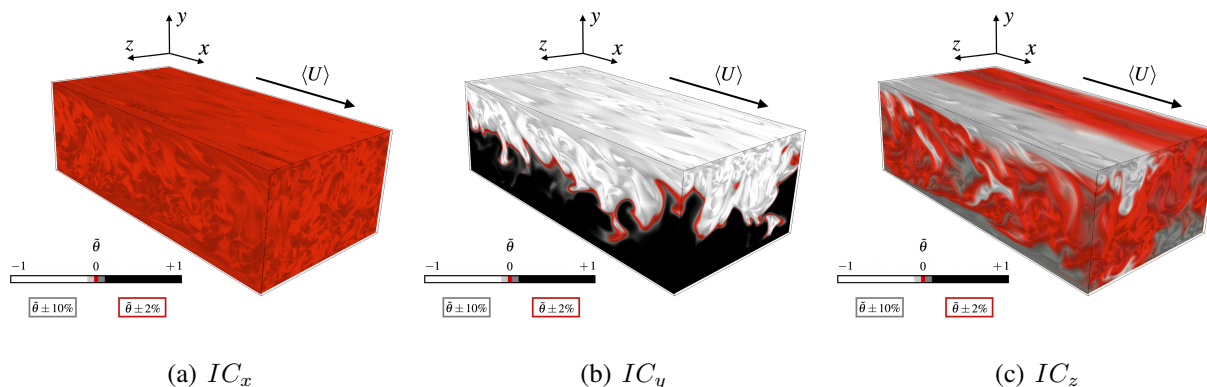


Figure 6: Concentration distributions generated at $\tau = 7$ by the action of the same turbulent channel flow on the three scalar-field initial conditions. (Imagery generated using VAPOR, www.vapor.ucar.edu).

From this figure, it is readily observed that the scalar field resulting from the IC_x initial condition is the best mixed, whereas that resulting from the IC_y initial condition is the least mixed. This is already an intriguing result and indicates that the initial conditions can strongly influence the subsequent mixing. Moreover, it is worth reiterating that all three scalar-field initial conditions were comprised of equal parts “black fluid” (i.e., scalar with an initial concentration $\tilde{\theta} = +1$) and “white fluid” (i.e., scalar with an initial concentration $\tilde{\theta} = -1$). Thus, one can already conclude that the rate at which mixing will occur in such an inhomogeneous flow (as is the flow in all

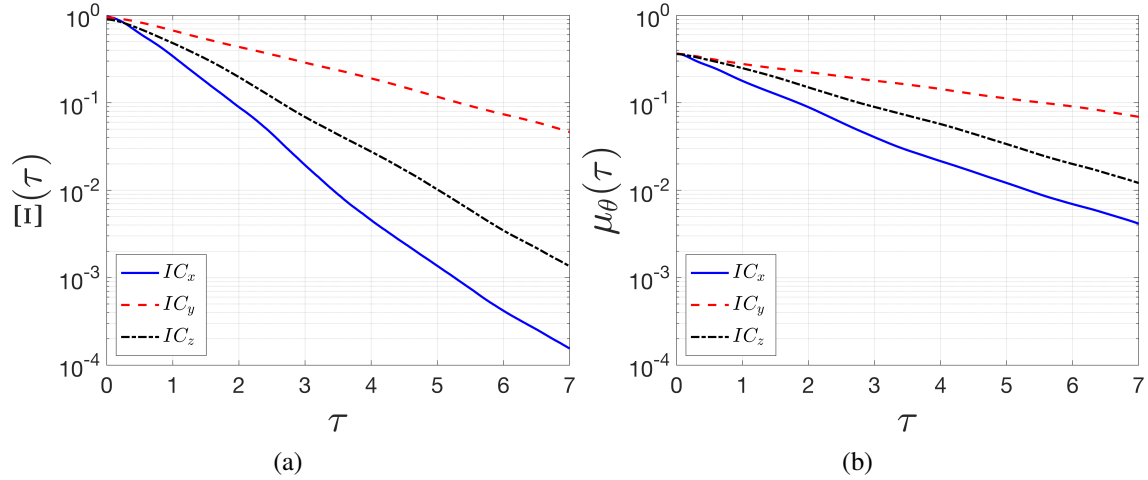


Figure 7: Time evolution of the unmixedness parameter (a) and the mix-norm (b) for the three scalar fields resulting from the three initial conditions.

real devices) is highly dependent on the initial configuration of the two quantities being mixed. Whereas the mixing of the scalar field could be studied qualitatively, using visualizations similar to those of figure 6 evaluated at different times, the remainder of this work takes a more quantitative approach by analyzing the evolution of statistics of the scalar field to quantify the mixing.

To quantify the mixing, we plot the time-evolution of the unmixedness parameter (Ξ) and the mix-norm (μ_θ) for the three scalar-field initial conditions in figure 7. One observes that the unmixedness starts very close to its maximum value of 1, whereas the initial values for the mix-norm fall between 0.3 and 0.4 (because the latter metric depends on the initial geometry of the scalar field). However, shortly after the velocity field starts mixing the scalar field, the time-evolution of both mixing metrics follows a similar pattern; i.e., the evolution of both Ξ and μ_θ decays exponentially with time, with the most efficient stirring and mixing (i.e., fastest rates of decay of Ξ and μ_θ) occurring for the IC_x case and the slowest for the IC_y case.

Recall that the unmixedness parameter, Ξ , is a measure of molecular mixing (primarily a small-scale feature) only, whereas the mix-norm, μ_θ , is a multiscale measure which accounts for molecular mixing and stirring (primarily a large-scale feature). The similar patterns of exponential decay of Ξ and μ_θ in time suggest that either the process of molecular mixing evolves in a manner similar to the evolution of combined molecular mixing and stirring, or that the effects of stirring

are only significant at early times.

To further interpret these results, it can be shown that the slopes of Ξ from figure 7(a) are directly related to the rate at which the scalar variance is destroyed as the flow evolves from an unmixed to a mixed state. A mathematical relationship between the unmixedness and the (volume-averaged) scalar variance can be derived by noting that (for a closed system) the mean scalar concentration, Θ , is a constant, and equation 7 can be rearranged in the form:

$$\Theta(1 - \Theta)\Xi = \langle \theta^2 \rangle_V.$$

Taking the time derivative of both sides, the resulting equation is:

$$\Theta(1 - \Theta) \frac{\partial \Xi}{\partial t} = \frac{\partial \langle \theta^2 \rangle_V}{\partial t}.$$

Lastly, invoking the scalar variance budget to substitute in for $\partial \langle \theta^2 \rangle_V / \partial t$ and recalling that $\partial \langle \cdot \rangle_V / \partial x_i = 0$ (such that the scalar variance budget reduces to $\partial \langle \theta^2 \rangle_V / \partial t = -2 \langle \varepsilon_\theta \rangle$), the time derivative of the unmixedness parameter can be directly related to the scalar dissipation rate by the equation:

$$\Theta(1 - \Theta) \frac{\partial \Xi}{\partial t} = -2 \langle \varepsilon_\theta \rangle_V. \quad (16)$$

The volume-averaged scalar dissipation rate can then be written in terms of the unmixedness parameter as follows:

$$\langle \varepsilon_\theta \rangle_V = -\frac{1}{2} \Theta(1 - \Theta) \frac{\partial \Xi}{\partial t} \quad (17)$$

Given the relationship between the evolution of the unmixedness to scalar dissipation rate derived above, it is logical to examine the evolutions of the (volume-averaged) scalar dissipation rates ($\langle \varepsilon_\theta \rangle$) corresponding to the fields with the three initial conditions as a function of time (see figure 8). The evolution of $\langle \varepsilon_\theta \rangle$ is both qualitatively and quantitatively (given the derivation in equation 17) similar to the evolution of Ξ . The dissipation rates decrease at rates dependent upon

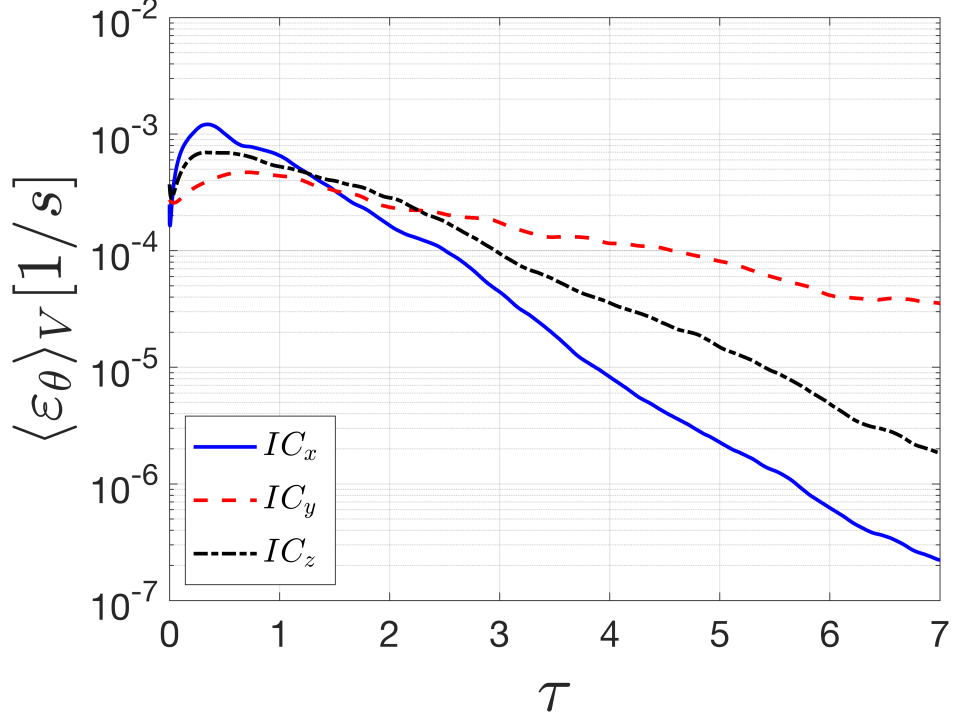


Figure 8: Time-evolution of the volume-averaged (i.e., $\langle \cdot \rangle = \langle \cdot \rangle_{x,y,z} = \langle \cdot \rangle_V$) scalar dissipation rates for the scalar fields resulting from the three initial conditions.

the initial conditions of the scalar field, with the the fastest decrease in $\langle \varepsilon_\theta \rangle$ occurring for IC_x , corresponding to the most efficient mixing, and the slowest corresponding to IC_y . At shorter times, $\langle \varepsilon_\theta \rangle$ increases, presumably due to the stretching and stirring of the interface between the two (i.e., the “black” and “white”) scalar fields, which results in a production of $\langle \varepsilon_\theta \rangle$. This is in contrast with the short-time evolution of both Ξ and μ_θ , which are both monotonically decreasing functions of time for all values of τ . Note that the values of $\langle \varepsilon_\theta \rangle$ for the IC_x and IC_z cases peak around $\tau \approx 1/3$, whereas the peak in $\langle \varepsilon_\theta \rangle$ for the IC_y case occurs later, around $\tau \approx 2/3$. Furthermore, the highest peak of $\langle \varepsilon_\theta \rangle$ occurs for IC_x , indicating the largest production of the scalar dissipation rate, whereas the smallest peak occurs the IC_y initial condition.

The relationship between the unmixedness parameter and the volume-averaged scalar dissipation rate given by equation 17 can also be observed in figure 9. The values of the scalar dissipation rates in figure 8 can be exactly related to the evolution of the unmixedness parameters in figure 7(a). The peak values for $\langle \varepsilon_\theta \rangle_V$ correspond to the locations of maximum slopes (i.e., fastest rates

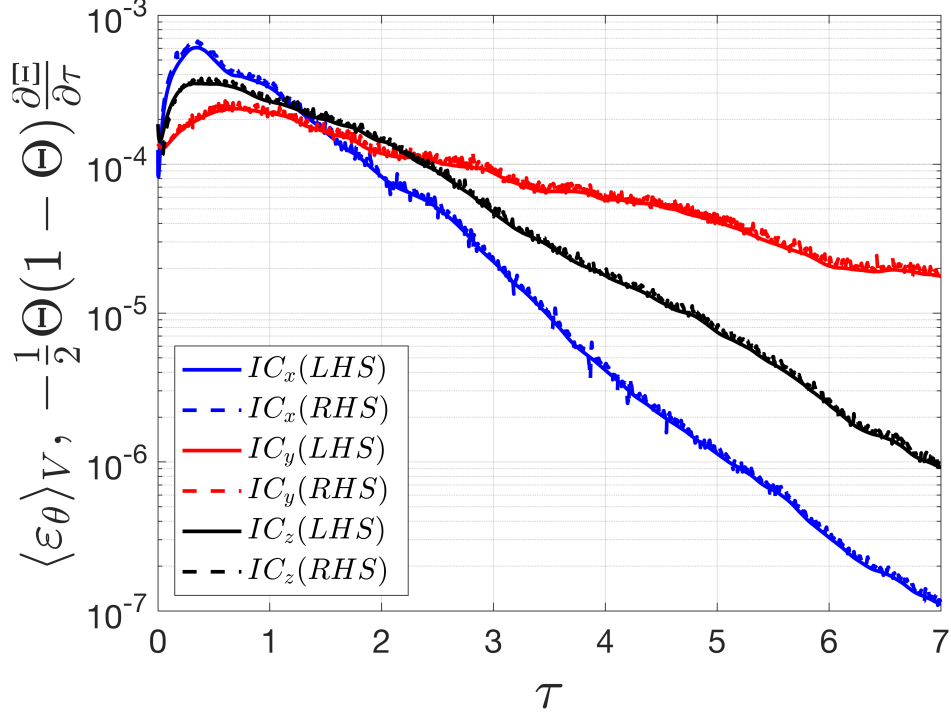


Figure 9: Comparisons of the left hand side (LHS) and right hand side (RHS) of equation 17 for the scalar fields resulting from the three initial conditions.

of decay) of the unmixedness parameter. As $\langle \varepsilon_\theta \rangle_V$ tends to zero at larger values of τ , the rate at which the scalar variance is destroyed (i.e., the rate of change of the unmixedness parameter) begins to slow down, with the IC_x case corresponding to the slowest rate of scalar variance destruction. The larger values of $\langle \varepsilon_\theta \rangle_V$ for case IC_y after the peaks observed in figure 8 depict how the scalar field resulting from that initial condition is the furthest from the mixed state.

Based on the evolution of $\langle \varepsilon_\theta \rangle$ over time, one can hypothesize that the rate at which the scalar variance is destroyed increases initially as a result of the initial interface being stretched and stirred by the flow for all three initial conditions. After a maximum rate of destruction of the scalar variance has been achieved, there is a monotonic decay in the rate of scalar variance destruction for all three initial conditions as the concentration distributions of the three scalar fields approach a mixed state with increasing time. Ultimately, the value of the scalar dissipation rate will tend to zero because there will be no scalar variance remaining that can be destroyed.

4.3.2 Scalar Variance Budget

To better understand the evolution of $\langle \varepsilon_\theta \rangle$ presented in figure 8, we start by studying the scalar variance budget (equation 5), which describes the contributions of different physical mechanisms involved in the evolution of the scalar variance. These mechanisms involve the mean, turbulent, and molecular transports of the scalar variance, in addition to its production and destruction. It should be noted that $\langle \varepsilon_\theta \rangle$ appears explicitly as a term in the scalar variance budget, as it quantifies the rate of destruction of the scalar variance. Thus, analysis of all the terms in the scalar variance budget will provide further insight into the physical processes that contribute to the evolution of the scalar variance.

To this end, figure 10 plots the contributions of the terms in the budget of $\langle \frac{1}{2}\theta^2 \rangle$. To assist the reader, a legend corresponding to the budget's six terms is also provided in table 1. The first observation to be made from figure 10 is that the rate of change in time of the scalar variance (i) is dominated by the production (v) and destruction (vi) of $\langle \frac{1}{2}\theta^2 \rangle$. The production of the scalar variance results from the stretching of the interface, which creates/enhances scalar gradients, thus increasing the scalar variance at early times, as indicated by the increase in term (i) of the scalar variance budget.

A second set of observations from figure 10 is drawn by considering the relative magnitudes of the terms for the different initial conditions. One observes that the largest peak for the production of the scalar variance (i.e., term (v)) occurs for IC_x , while the smallest peak occurs for IC_y . Furthermore, the largest peak in the destruction of the scalar variance (i.e., $\langle \varepsilon_\theta \rangle$) also occurs for IC_x , with the smallest peak again being associated with the IC_y initial condition. The highest magnitude for $\langle \varepsilon_\theta \rangle$ observed for the IC_x initial condition in figure 10 is consistent with the highest peak observed in the volume-averaged scalar dissipation rate in figure 8. Similarly, the smallest magnitude of $\langle \varepsilon_\theta \rangle$ observed in the scalar variance budget is consistent with the smallest observed peak in the volume-averaged plot of $\langle \varepsilon_\theta \rangle$ as seen in figure 8.

Lastly, it becomes apparent from figure 10 that the production and destruction of the scalar

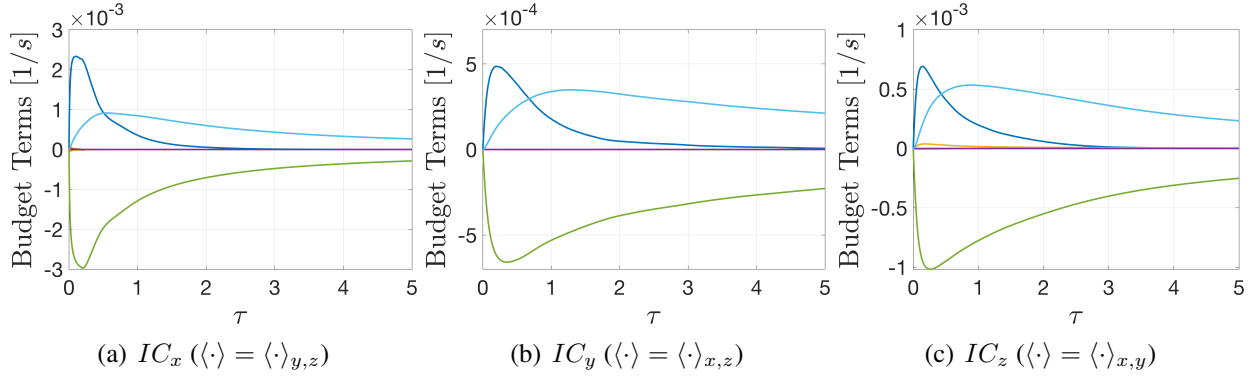


Figure 10: Evolution in time of the space- and time-averages of all 6 terms in the scalar variance budget in which statistical moments ($\langle \cdot \rangle$) are assessed in planes parallel to the initial location of the interface in the initial condition. (a) IC_x with $\frac{1}{L_x} \frac{1}{\tau} \int_0^{L_x} \int_0^\tau Term d\tau' dx$, (b) IC_y with $\frac{1}{2h} \frac{1}{\tau} \int_0^{2h} \int_0^\tau Term d\tau' dy$, and (c) IC_z with $\frac{1}{L_z} \frac{1}{\tau} \int_0^{L_z} \int_0^\tau Term d\tau' dz$. Note the different scales of the vertical axes.

Table 1: Legend for the various terms in the budget of the scalar variance.

Color	Term #	Term	Physical interpretation
	(i)	$\frac{\partial}{\partial t} \langle \frac{1}{2} \theta^2 \rangle$	time rate of change of $\langle \frac{1}{2} \theta^2 \rangle$
	(ii)	$U_j \frac{\partial}{\partial x_j} \langle \frac{1}{2} \theta^2 \rangle$	mean flow advection of $\langle \frac{1}{2} \theta^2 \rangle$
	(iii)	$\frac{\partial}{\partial x_j} \langle \frac{1}{2} u_j \theta^2 \rangle$	turbulent advection of $\langle \frac{1}{2} \theta^2 \rangle$
	(iv)	$-\alpha \frac{\partial^2}{\partial x_j^2} \langle \frac{1}{2} \theta^2 \rangle$	molecular transport of $\langle \frac{1}{2} \theta^2 \rangle$
	(v)	$\langle u_j \theta \rangle \frac{\partial \theta}{\partial x_j}$	production of $\langle \frac{1}{2} \theta^2 \rangle$
	(vi)	$\alpha \langle \frac{\partial \theta}{\partial x_j} \frac{\partial \theta}{\partial x_j} \rangle$	destruction of $\langle \frac{1}{2} \theta^2 \rangle$ (i.e., $\langle \varepsilon_\theta \rangle$)

variance is most dominant at early times, when each of the three systems are the least mixed. Although scalar variance increases at early times due to a larger production of $\frac{1}{2} \langle \theta^2 \rangle$ than its destruction, its rate of change goes to zero once the production and destruction of $\frac{1}{2} \langle \theta^2 \rangle$ become balanced at later times. When spatially averaged over the respective direction of inhomogeneity, the contributions from mean, molecular, and turbulent transport are non-existent for all three scalar-field initial conditions. Consequently, a long term equilibrium exists in figure 10 between the production and destruction of $\frac{1}{2} \langle \theta^2 \rangle$. As the systems approach a uniformly mixed state, the production and destruction curves begin to asymptotically decay to zero.

4.3.3 Scalar Dissipation Rate Budget

A better understanding of the evolution of $\langle \varepsilon_\theta \rangle$ can be achieved by analyzing the terms in the scalar dissipation rate budget (equation 6). Whereas the scalar variance budget describes the phenomena impacting the evolution of the scalar variance, the scalar dissipation rate budget describes the phenomena involved in the evolution of $\langle \varepsilon_\theta \rangle$. An analysis of the terms in the scalar dissipation rate budget will therefore provide insight into the contributions of various physical processes involved in the evolution of $\langle \varepsilon_\theta \rangle$.

To further investigate the evolutions of $\langle \varepsilon_\theta \rangle$ depicted in figure 8, figure 11 plots the contributions of the terms in the budget of $\langle \varepsilon_\theta \rangle$. To once again assist the reader, a legend corresponding to the 9 terms of equation 6 is given in table 2. Multiple observations can be made from the plots therein. For $\tau > 1$, $\langle \varepsilon_\theta \rangle$ is dominated by a balance between the production of $\langle \varepsilon_\theta \rangle$ arising from turbulent vortex stretching, and dissipation of $\langle \varepsilon_\theta \rangle$ by molecular processes, as first predicted by Corrsin (1953). However, further details bear noting. Firstly, when considering the relative magnitudes of the various terms for the different initial conditions, it is clear that the magnitudes of the terms for the IC_x condition are the largest, followed by those corresponding to the IC_z initial condition. Those corresponding to the IC_y initial condition are the smallest. Using the peak value of the molecular dissipation of $\langle \varepsilon_\theta \rangle$ (i.e., term (ix) , light green line) as a reference, its value for IC_x is 4×10^{-5} , for IC_z is 2×10^{-5} , and for IC_y is $1 \times 10^{-5} s^{-2}$. Thus the larger values of all terms in the scalar field arising from the IC_x initial condition lead to the largest peaks of $\langle \varepsilon_\theta \rangle$, as well as the fastest decay rates of $\langle \varepsilon_\theta \rangle$, consistent with figure 8. Moreover, the converse holds for IC_y , which experiences the lowest peak value of $\langle \varepsilon_\theta \rangle$ and slowest decay rates. Secondly, one can observe in figure 11 that the two dominant terms (production of $\langle \varepsilon_\theta \rangle$ by turbulent vortex stretching and molecular dissipation of $\langle \varepsilon_\theta \rangle$) peak at later times for IC_y (at $\tau > 1$) than they do for the IC_x and IC_z cases (which peak at $\tau < 1$). This behaviour is also consistent with the evolutions of $\langle \varepsilon_\theta \rangle$ in figure 8, noted above.

To further investigate the budget of the scalar dissipation rate for the three initial conditions,

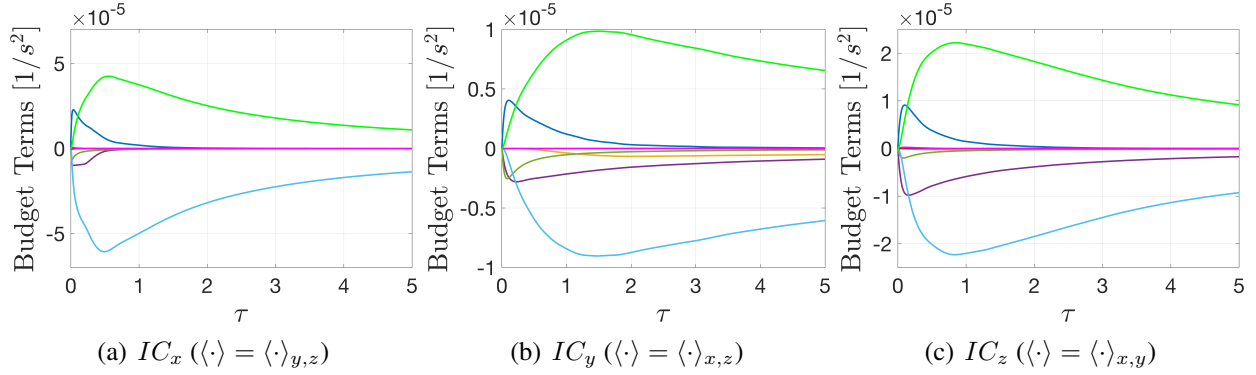


Figure 11: Evolution in time of the space- and time-averages of all 9 terms in the scalar dissipation rate budget in which statistical moments ($\langle \cdot \rangle$) are assessed in planes parallel to the initial location of the interface in the initial condition. (a) IC_x with $\frac{1}{L_x} \frac{1}{\tau} \int_0^{L_x} \int_0^\tau Term d\tau' dx$, (b) IC_y with $\frac{1}{2h} \frac{1}{\tau} \int_0^{2h} \int_0^\tau Term d\tau' dy$, and (c) IC_z with $\frac{1}{L_z} \frac{1}{\tau} \int_0^{L_z} \int_0^\tau Term d\tau' dz$. Note the different scales of the vertical axes.

the time evolution of terms when spatially averaged over a single y - z plane is plotted in figure 12. Note that the plane over which the spatial averaging is performed in figure 12 is parallel to the initial interface between the “black” and “white” fluids in the IC_x case, and located at the mid-plane of the channel in the x -direction (i.e., $x/L_x = 0.5$), i.e., the location of one of the two interfaces between the “black” and “white” fluids at $\tau = 0$ for IC_x . In figure 12, it is first worth noting the qualitative similarities of the evolutions of the terms in the $\langle \varepsilon_\theta \rangle$ budget for the IC_y and IC_z initial conditions. These two subfigures exhibit similar behaviours due to the absence of terms associated with spatial gradients of statistical moments in the directions of the averaging in the respective figures. We also note that analogous similarities are observed when reproducing the equivalent of figure 12, but spatial averaging in the other two (x - z and x - y) mid-planes (see figures 13 and 14). Plotted in figures 13 and 14 are the temporal evolutions of the scalar dissipation rate budget terms when averaged along x - z and x - y planes, respectively, at the other two mid-planes of the channel. The averaging schemes used ensure that the relevant budget terms are conserved for IC_y in the case of x - z averaging, and for IC_z in the case of x - y averaging. In contrast to figures 12(b) and 12(c), figure 12(a) is dominated at early times by mean-flow advection of $\langle \varepsilon_\theta \rangle$ and turbulent advection of $\langle \varepsilon_\theta \rangle$. This will be further discussed with respect to figure 15, which follows.

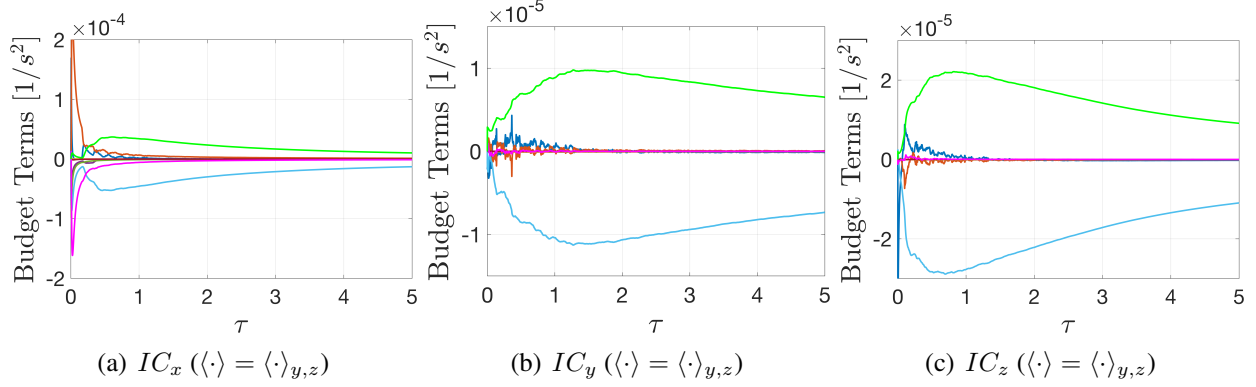


Figure 12: Temporal averages of the time-averages of all 9 terms in the scalar dissipation rate budget in which statistical moments $\langle \cdot \rangle$ are assessed on the y - z plane at $x/L_x = 0.50$, i.e., $\frac{1}{\tau} \int_0^\tau Term d\tau'$, where all averages $\langle \cdot \rangle$ in $Term$ are given by $\langle \cdot \rangle = \langle \cdot \rangle_{y,z}$.

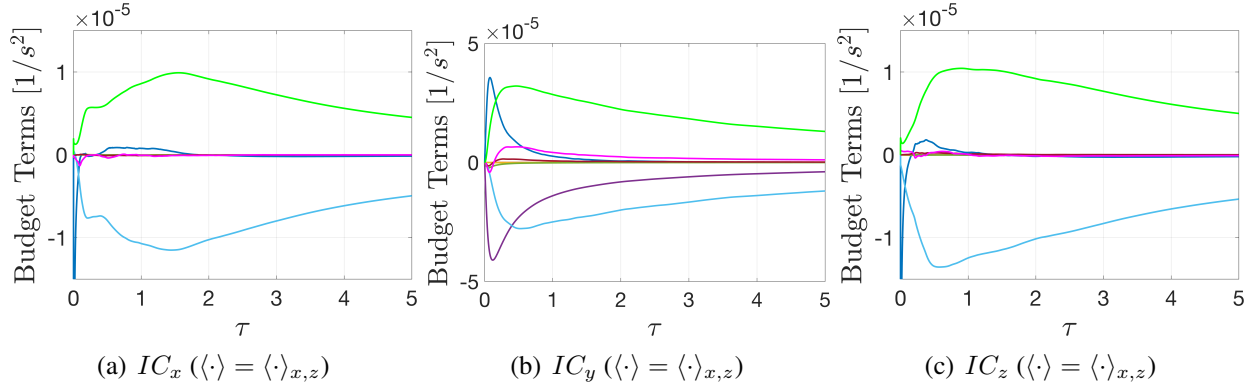


Figure 13: Evolution in time of the time-averages of all 9 terms in the scalar dissipation rate budget in which statistical moments $\langle \cdot \rangle$ are assessed on the x - z plane at $y/h = 1$, i.e., $\frac{1}{\tau} \int_0^\tau Term d\tau'$, where all averages $\langle \cdot \rangle$ in $Term$ are given by $\langle \cdot \rangle = \langle \cdot \rangle_{x,z}$.

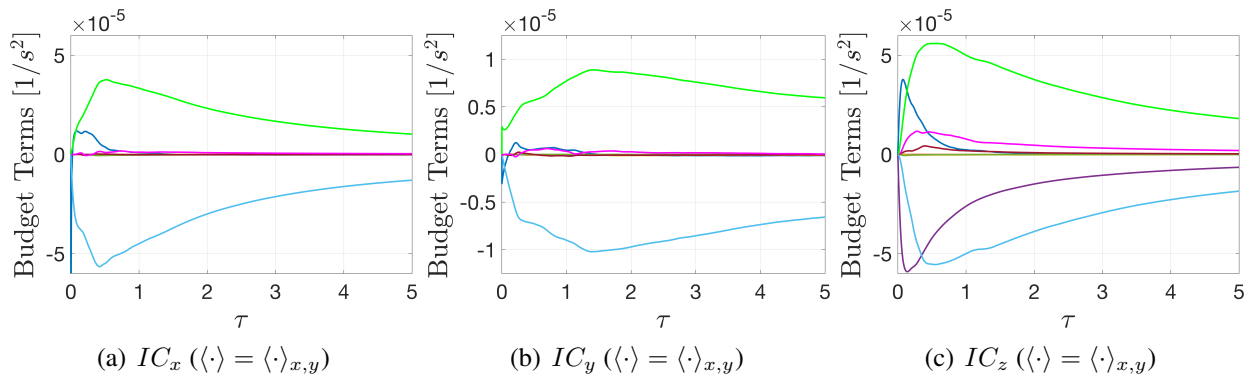


Figure 14: Evolution in time of the time-averages of all 9 terms in the scalar dissipation rate budget in which statistical moments $\langle \cdot \rangle$ are assessed on the x - y plane at $z/L_z = 0.50$, i.e., $\frac{1}{\tau} \int_0^\tau Term d\tau'$, where all averages $\langle \cdot \rangle$ in $Term$ are given by $\langle \cdot \rangle = \langle \cdot \rangle_{x,y}$.

Table 2: Legend for the various terms in the budget of the scalar dissipation rate.

Color	Term #	Term	Physical interpretation
	(i)	$\frac{\partial}{\partial t} \langle \varepsilon_\theta \rangle$	time rate of change of $\langle \varepsilon_\theta \rangle$
	(ii)	$\langle U_j \rangle \frac{\partial}{\partial x_j} \langle \varepsilon_\theta \rangle$	mean flow advection of $\langle \varepsilon_\theta \rangle$
	(iii)	$2\alpha \frac{\partial \langle U_j \rangle}{\partial x_i} \langle \frac{\partial \theta}{\partial x_i} \frac{\partial \theta}{\partial x_j} \rangle$	production of $\langle \varepsilon_\theta \rangle$ by mean velocity gradients
	(iv)	$2\alpha \frac{\partial \langle T \rangle}{\partial x_j} \langle \frac{\partial u_j}{\partial x_i} \frac{\partial \theta}{\partial x_i} \rangle$	production of $\langle \varepsilon_\theta \rangle$ by mean scalar gradients
	(v)	$2\alpha \frac{\partial^2 \langle T \rangle}{\partial x_i \partial x_j} \langle u_j \frac{\partial \theta}{\partial x_i} \rangle$	mixed production of $\langle \varepsilon_\theta \rangle$
	(vi)	$2\alpha \langle \frac{\partial u_j}{\partial x_i} \frac{\partial \theta}{\partial x_i} \frac{\partial \theta}{\partial x_j} \rangle$	production of $\langle \varepsilon_\theta \rangle$ by turbulent vortex stretching
	(vii)	$-\alpha \frac{\partial^2}{\partial x_j \partial x_j} \langle \varepsilon_\theta \rangle$	molecular transport of $\langle \varepsilon_\theta \rangle$
	(viii)	$\frac{\partial}{\partial x_j} \langle u_j \varepsilon_\theta \rangle$	turbulent advection of $\langle \varepsilon_\theta \rangle$
	(ix)	$2\alpha^2 \langle \frac{\partial^2 \theta}{\partial x_i \partial x_j} \frac{\partial^2 \theta}{\partial x_i \partial x_j} \rangle$	molecular dissipation of $\langle \varepsilon_\theta \rangle$

To investigate the evolution of the terms in the $\langle \varepsilon_\theta \rangle$ budget that are *not* subjected to such an artefact as that discussed with respect to figure 12, figure 15 plots the evolution in time of the scalar dissipation rate budget terms assessed on the mid-plane corresponding to the initial location of the interface for the three initial conditions. It reveals that figure 15(a), which corresponds to the IC_x initial condition (figure 12(a)), is significantly different from those corresponding to IC_y (15(b)) and IC_z (15(c)), which are quite similar (figures 13(b) and 14(c), respectively). Whereas the dominant terms in figures 15(b) and 15(c) are the molecular dissipation of $\langle \varepsilon_\theta \rangle$, the production of $\langle \varepsilon_\theta \rangle$ by turbulent vortex stretching, production of $\langle \varepsilon_\theta \rangle$ by mean scalar gradients, the rate of change of $\langle \varepsilon_\theta \rangle$ with time, and turbulent advection of $\langle \varepsilon_\theta \rangle$, figure 15(a) is distinctly different. Of particular note is the importance played by mean-flow advection of $\langle \varepsilon_\theta \rangle$ at early times, which is dominant for $\tau < 0.2$, and balanced by turbulent advection of $\langle \varepsilon_\theta \rangle$ for IC_x . Given that fully developed turbulent channel flow must be unidirectional, the absence of the mean-flow advection term in the other directions is to be expected. However, the early dominance of this term is noteworthy. In this respect, consideration of the evolution in time of the interface(s) between the “black” and “white” fluids is beneficial. For the IC_y case, the $\langle \Theta \rangle = 0$ plane will not change in time and

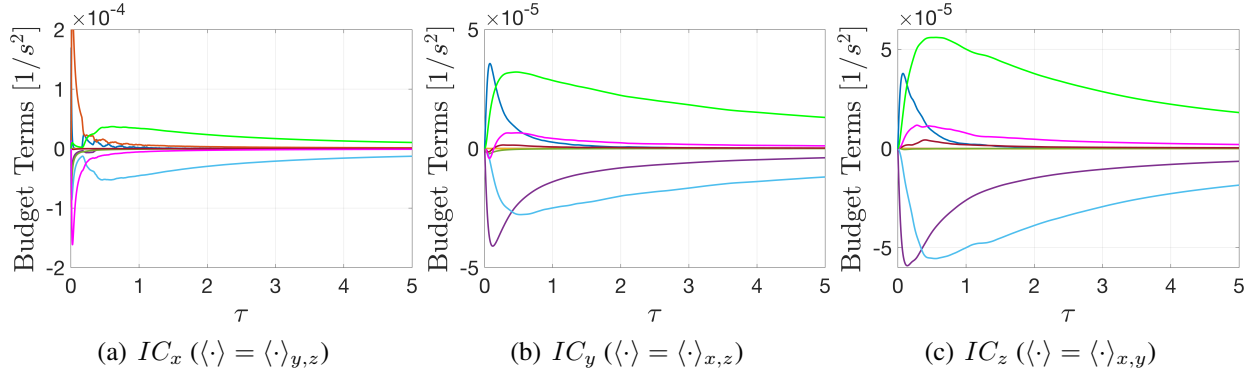


Figure 15: Evolution in time of the time-averages of all 9 terms in the scalar dissipation rate budget in which statistical moments $\langle \cdot \rangle$ are assessed on the mid-plane corresponding to the initial location of the interface in the initial condition: $\frac{1}{\tau} \int_0^\tau Term d\tau'$. (a) IC_x with statistical moments evaluated over the y - z plane at $x/L_x = 0.50$, (b) IC_y with statistical moments evaluated over the x - z plane at $y/h = 1$, and (c) IC_z with statistical moments evaluated over the x - y plane at $z/L_z = 0.50$.

will be advected along the $y/h = 1$ plane as the flow evolves, but remaining at the same location as the initial interface. However, the evolution of the scalar field in time is quite different for IC_x . The interface remains “anchored” to the walls due to the no-slip condition, and is strongly stretched in the x -direction by the mean flow, while being stirred by the turbulence. Thus as the interface is advected downstream, it can “blow by” a given downstream location multiple times. This effect can be observed by the oscillations in the unsteady term (dark blue line), and to a lesser degree the mean flow advection terms (red line) in figure 15(a). It is worth noting that the period of the observed oscillation is indeed equal to half of the channel’s “flow-through” time (i.e., $\frac{1}{2}\tau_{FT} \equiv \frac{1}{2}(L_x/\langle U \rangle_{y/h=1})u_\tau/h = 0.17$). With respect to IC_z , the $\Theta = 0$ plane will be advected downstream the mid-plane of the channel ($z = 0.5L_z$), although its top and bottom edges will remain anchored to the walls of the channel, thus emulating aspects of both IC_x and IC_y . The anchoring of the interfaces to the walls also subjects them to strong turbulent activity that is encountered in the near-wall region. As such, IC_x and IC_z experience enhanced scalar mixing due to the strong turbulent activity arising from the anchoring of the interfaces to the walls.

Given that the results in figure 15 are all averages taken at the three midplanes of the channel, they are somewhat anomalous. For example, when averaging in the x - and z -directions at $y/h = 1$

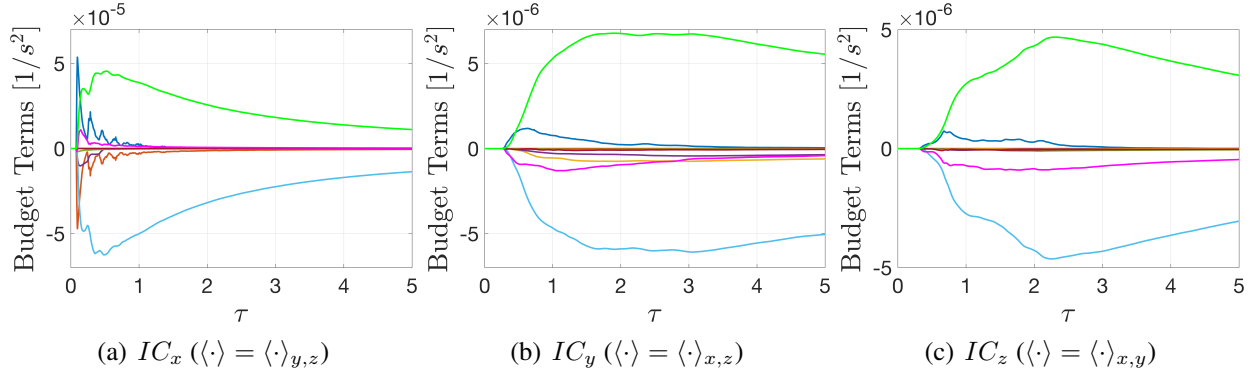


Figure 16: Evolution in time of the time-averages of all 9 terms in the scalar dissipation rate budget in which statistical moments $\langle \cdot \rangle$ are assessed in planes parallel to the initial location of the interface in the initial condition, but *away from the mid-plane*: $\frac{1}{\tau} \int_0^\tau Term d\tau'$. (a) IC_x with statistical moments evaluated over the y - z plane at $x/L_x = 0.25$, (b) IC_y with statistical moments evaluated over the x - z plane at $y/h = 0.5$, and (c) IC_z with statistical moments evaluated over the x - y plane at $z/L_z = 0.25$.

(as is the case in figure 15(b)), there can be no contribution to $\langle \varepsilon_\theta \rangle$ arising from production by the mean velocity gradient, because $\partial \langle U \rangle / \partial y = 0$ at that one location (and no other). Thus it bears investigating the budget of the scalar dissipation rate for the three initial conditions at non-mid-plane locations. To this end, the evolutions of the terms in the budget of the scalar dissipation rate are plotted for IC_x spatially averaged over a y - z plane located at $x/L_x = 0.25$ in figure 16(a), for IC_y spatially averaged over an x - z plane located at $y/h = 0.5$ in figure 16(b), and for IC_z spatially averaged over an x - y plane located at $z/L_z = 0.25$ in figure 16(c). The aforementioned periodic passing of the interface over the measurement plane for the IC_x case is even more prominent in figure 16(a). However, figures 16(b) and 16(c) also reveal another phenomenon that explains the slower evolution of $\langle \varepsilon_\theta \rangle$ for the IC_y and IC_z cases. In these two non-mid-plane cases, one observes an initial period of “inactivity.” The initial period in which the terms in the budget of $\langle \varepsilon_\theta \rangle$ are effectively zero results from the interface having not yet “reached” the measurement location. In these two cases, the interface can only travel laterally by the action of the turbulence, given that there is no mean velocity in the y - and z -directions. This phenomenon i) is not observed for the IC_x case, because the interface can be advected by the non-zero mean flow, and ii) further explains the slower evolution of $\langle \varepsilon_\theta \rangle$ for the IC_y and IC_z cases, given that regions located increasingly far

away from the interface experience a delay before they begin to mix. This latter effect therefore serves to retard the total mixing, because the interface surface is not normal to the mean velocity vector.

4.4 Results Summary

The evolutions of the mixing metrics (unmixedness parameter and mix-norm) show a clear dependence on the scalar-field initial conditions. The case where the initial interface is normal to the mean velocity gradient (IC_x) experiences the fastest mixing, whereas IC_y , in which the initial interface is parallel to the velocity gradient and is not anchored to the walls, experiences the slowest mixing. The relationship established between the mixing metrics and the volume-averaged scalar dissipation rate shows that the initial rise in $\langle \varepsilon_\theta \rangle_V$ directly corresponds to an increase in the rate at which the unmixedness tends to zero. The decay of $\langle \varepsilon_\theta \rangle_V$ after the peak indicates further that IC_x experiences the fastest decrease in the rate of scalar variance destruction, and approaches the mixed state fastest out of the three initial conditions.

The evolution of $\langle \varepsilon_\theta \rangle$ is first explained by examining the scalar variance budget, which indicates that the magnitude of the production and destruction of the scalar variance is the highest for the IC_x case. Furthermore, an analysis of the scalar dissipation rate budget provides additional insight into the fastest mixing observed for the IC_x case. The largest magnitudes of the production and destruction of $\langle \varepsilon_\theta \rangle$ correspond to the largest peak and decay of $\langle \varepsilon_\theta \rangle$ for IC_x . Another key factor contributing to the fastest mixing is the strong stretching of the initial interface by the mean velocity gradient in IC_x , whereas the parallel orientation of the interfaces with respect to the mean velocity vector in IC_y and IC_z makes them subject to a period of inactivity away from the location of the initial interface. Lastly, the enhanced mixing by the strong near-wall turbulent activity further plays a role in the fastest mixing observed in IC_x .

5 CONCLUSION

The last section of this thesis is divided into two subsections, which summarize the findings of the research, followed by a brief discussion of future work to extend the results presented herein.

5.1 Summary

The motivation behind the present work was a lack of understanding of the effects of scalar-field initial conditions on the evolution of the scalar concentration. Very often in both natural and engineering applications, it is desirable to either promote or delay the mixing of a scalar in a turbulent flow. To that extent, it is beneficial to better understand the role of scalar-field initial conditions in the evolution of the field from an unmixed state to a mixed one.

Direct numerical simulations were conducted for three different scalar-field initial conditions to study their effects on the evolutions of the mixing metrics and the scalar variance and scalar dissipation rate budgets. The flow considered in this work was a fully-developed turbulent channel flow, to provide relevance with the abundance of inhomogeneous flows encountered in the real world. The hydrodynamic field was simulated using a public spectral code entitled CHANNELFLOW, while the scalar fields were simulated using a flux integral code entitled 3DFLUX.

Results of the DNSs showed that there was a clear dependence of the rate of mixing on the scalar-field initial conditions. Evolutions of the unmixedness parameter and the mix-norm in time showed that the case with the initial scalar interface aligned normal to the direction of the mean velocity vector (IC_x) experienced the fastest mixing of the three initial conditions. The case where the initial interface was aligned parallel to the mean velocity vector and was not anchored to the walls (IC_y) experienced the slowest mixing.

To further understand the evolution of the unmixedness, it was mathematically related to the volume-averaged scalar dissipation rate by showing that its rate of change with time was directly proportional to $\langle \varepsilon_\theta \rangle_V$. An increase in $\langle \varepsilon_\theta \rangle_V$ was observed at early times, presumably due to the stretching of the interface, with a decay of the scalar dissipation rate following the peaks. The

largest peak of $\langle \varepsilon_\theta \rangle_V$ for the IC_x case corresponded to the fastest rate of destruction of scalar variance observed across all three cases. As the mixing progressed, the values of $\langle \varepsilon_\theta \rangle_V$ tended towards zero, with IC_x approaching the mixed state sooner than the other initial conditions.

Analysis of the scalar variance budget provided further insight into the mixing resulting from the different initial conditions. It was found that the magnitudes of production and destruction of $\langle \frac{1}{2}\theta^2 \rangle$ were highest for IC_x , and lowest for IC_y . Furthermore, the production and destruction terms were most dominant at early times ($\tau < 1$) and asymptotically decayed to zero as the systems approached a mixed state.

Analysis of the terms in the budget of the scalar dissipation rate showed that the magnitude of the terms was consistent with both large values of $\langle \varepsilon_\theta \rangle$ and rapid decay rates of $\langle \varepsilon_\theta \rangle$. Once again, the magnitudes of the production(s) and destruction of $\langle \varepsilon_\theta \rangle$ were the highest for the IC_x case and the lowest for IC_y . The strong stretching of the initial interface by the mean velocity gradient was a key factor in promoting the production of $\langle \varepsilon_\theta \rangle$ in IC_x . Furthermore, a period of inactivity away from the initial locations of the interfaces for IC_y and IC_z was observed and attributed to the lack of mean-flow advection normal to the initial interface. Lastly, anchoring of the interfaces to the walls for IC_x and IC_z subjected them to strong near-wall turbulent activity and enhanced the mixing.

These observations suggest that the orientation of the initial interface with respect to the mean velocity vector plays a key role in the evolution of the scalar field. The mixing and stirring that occurs therein is influenced by the stretching (or lack thereof) of the initial interface and also by the action of the near-wall turbulent activity. The mechanisms that contribute to the production and destruction of the scalar dissipation rate greatly benefit from having the interface being anchored to the walls while being strongly stretched by the mean flow. Thus, it is recommended that for a wall-bounded flow, the scalar interfaces should be aligned normal to the direction of the mean velocity vector to enhance the stretching of the interface and thus promote scalar mixing.

5.2 Future Work

Future work should further investigate the initial period of the mixing process (i.e., $\tau < 1$). Such an analysis could provide insight into the rate of increase observed in $\langle \varepsilon_\theta \rangle$ in the initial phases of the mixing during which the scalar interface is being stretched. It would also be of interest to investigate the effects of scalar-field initial conditions on the ensuing mixing in other canonical flows. The most relevant one might be the turbulent jet, given the role it plays in various combustion systems, in which scalar mixing plays a crucial role to the efficiencies of the overall system and process.

References

- Abe, H., Kawamura, H., and Matsuo, Y. (2001). Direct numerical simulation of a fully developed turbulent channel flow with respect to the Reynolds number dependence. *J. Fluid. Eng. - T. ASME*, 123:382–393.
- Batchelor, G. (1959). Small-scale variation of convected quantities like temperature in turbulent fluid. Part 1. General discussion and the case of small conductivity. *J. Fluid Mech.*, 5:113–133.
- Beaulac, S. and Mydlarski, L. (2004a). Dependence on the initial conditions of scalar mixing in the turbulent wake of a circular cylinder. *Phys. Fluids*, 16:3161–3172.
- Beaulac, S. and Mydlarski, L. (2004b). Inverse structure functions of temperature in grid-generated turbulence. *Phys. Fluids*, 16:2126–2129.
- Berajeklian, A. and Mydlarski, L. (2011). Simultaneous velocity-temperature measurements in the heated wake of a cylinder with implications for the modeling of turbulent passive scalars. *Phys. Fluids*, 23:055107.
- Canuto, C., Hussaini, M., Quateroni, A., and Zhang, T. (1988). *Spectral Methods in Fluid Dynamics*. Springer-Verlag.
- Corrsin, S. (1951). On the spectrum of isotropic temperature fluctuations in an isotropic turbulence. *J. Appl. Phys.*, 22 (4):469–473.
- Corrsin, S. (1953). Remarks on turbulent heat transfer. *Proc. Iowa Thermodynamics Symposium, State University of Iowa, Iowa City*, pages 5–30.
- Danckwerts, P. V. (1952). The definition and measurement of some characteristics of mixtures. *Appl. Sci. Res.*, A3:279.
- Dimotakis, P. (2000). The mixing transition in turbulent flows. *J. Fluid Mech.*, 409:69–98.

- Dimotakis, P. E. and Miller, P. (1990). Some consequences of the boundedness of scalar fluctuations. *Phys. Fluids A*, 2:1919.
- Eggl, M. and Schmid, P. (2020). Mixing enhancement in binary fluids using optimised stirring strategies. *J. Fluid Mech.*, 899:A24.
- Eggl, M. and Schmid, P. (2022). Mixing by stirring: Optimizing shapes and strategies. *Phys. Rev. Fluids*, 7:073904.
- Foures, D., Caulfield, C., and Schmid, P. J. (2014). Optimal mixing in two-dimensional plane Poiseuille flow at finite Péclet number. *J. Fluid Mech.*, 748:241–277.
- Germaine, E., Mydlarski, L., and Cortelezzi, L. (2013). 3DFLUX: A high-order fully three-dimensional flux integral solver for the scalar transport equation. *J. Compute. Phys.*, 240:121.
- Germaine, E., Mydlarski, L., and Cortelezzi, L. (2014). Evolution of the scalar dissipation rate downstream of a concentrated line source in turbulent channel flow. *J. Fluid. Mech.*, 749:227–274.
- Germaine, E., Mydlarski, L., and Cortelezzi, L. (2018). Persistence of local anisotropy of passive scalars in wall-bounded flows. *Phys. Rev. Fluids*, 3(1):014606.
- Gibson, J. F. (2010). Channelflow: A spectral Navier-Stokes simulator in C++, licensed under the GNU GPL, <http://channelflow.org/>. Technical report, University of New Hampshire.
- Gibson, J. F., Halcrow, J., and Cvitanović, P. (2008). Visualizing the geometry of state space in plane Couette flow. *J. Fluid Mech.*, 611:107–130.
- Gubanov, O. and Cortelezzi, L. (2009). Sensitivity of mixing optimization to the geometry of the initial scalar field. In Cortelezzi, L. and Mezić, I., editors, *Analysis and Control of Mixing with an Application to Micro and Macro Flow Processes*, pages 369–405. Springer, Vienna.

- Gubian, P., Stoker, J., Medvescek, J., Mydlarski, L., and Baliga, B. (2019). Evolution of wall shear stress with Reynolds number in fully developed turbulent channel flow experiments. *Phys. Rev. Fluids*, 4:074606.
- Hewes, A. and Mydlarski, L. (2021). Design of thermal-anemometry-based probes for the simultaneous measurement of velocity and gas concentration in turbulent flows. *Meas. Sci. Technol.*, 32:105305.
- Hewes, A. and Mydlarski, L. (2022). Simultaneous measurements of velocity, gas concentration, and temperature by way of thermal-anemometry-based probes. *Meas. Sci. Technol.*, 33:015301.
- Kolmogorov, A. (1941). The local structure of turbulence in incompressible viscous fluid for very large Reynolds numbers. *Dokl. Akad. Nauk SSSR*, 30:301–305.
- Lensvelt, R., Speetjens, M., and Nijmeijer, H. (2022). Fast fluid heating by adaptive flow reorientation. *Int. J. Therm. Sci.*, 180:107720.
- Lepore, J. and Mydlarski, L. (2009). Effect of the scalar injection mechanism on passive scalar structure functions in a turbulent flow. *Phys. Rev. Lett.*, 103:034501.
- Lin, Z., Thiffeault, J.-L., and Doering, C. R. (2011). Optimal stirring strategies for passive scalar mixing. *J. Fluid Mech.*, 675:465–476.
- Mathew, G., Mezić, I., and Petzold, L. (2005). A multiscale measure for mixing. *Physica D*, 211:23.
- Monin, A. and Yaglom, A. (1971). *Statistical Fluid Mechanics*. MIT Press.
- Obukhov, A. (1949). Structure of the temperature field in turbulent flows. *Akad. Nauk. SSSR*, 13:58–69.
- Patankar, S. (1980). *Numerical Heat Transfer and Fluid Flow*. London: Hemisphere Publishing Corporation.

- Pope, S. B. (2000). *Turbulent Flows*. Cambridge University Press, Cambridge, UK, edition.
- Pumir, A. (1994). A numerical study of the mixing of a passive scalar in three dimensions in the presence of a mean gradient. *Phys. Fluids*, 6:2118–2132.
- Richardson, L. (1922). *Weather Prediction by Numerical Process*. Cambridge University Press.
- Simens, M., Jiménez, J., Hoyas, S., and Mizuno, Y. (2009). A high-resolution code for turbulent boundary layers. *J. Comput. Phys.*, 228(11):4218–4231.
- Sreenivasan, K. (1991). On local isotropy of passive scalars in turbulent shear flows. *Proc. R. Soc. London, Ser. A*, 434:165–182.
- Tennekes, H. and Lumley, J. L. (1972). *A First Course in Turbulence*. The MIT Press, Cambridge, Massachusetts, and London, England, First edition.
- Thiffeault, J.-L. (2012). Using multiscale norms to quantify mixing and transport. *Nonlinearity*, 25:R1–R44.
- Vermach, L. and Caulfield, C. (2018). Optimal mixing in three-dimensional plane Poiseuille flow at high Péclet number. *J. Fluid Mech.*, 850:875–923.
- Warhaft, Z. (2000). Passive scalars in turbulent flows. *Annu. Rev. Fluid Mech.*, 32:203–240.
- Zang, T. (1991). On the rotation and skew-symmetric forms for incompressible flow simulations. *Appl. Numer. Math.*, 7:27–40.